



HAL
open science

Modeling the fretting fatigue endurance from partial to gross slip: the effect of debris layer

P. Arnaud, S. Fouvry

► **To cite this version:**

P. Arnaud, S. Fouvry. Modeling the fretting fatigue endurance from partial to gross slip: the effect of debris layer. *Tribology International*, 2020, 143, pp.106069. 10.1016/j.triboint.2019.106069 . hal-03093085

HAL Id: hal-03093085

<https://hal.science/hal-03093085>

Submitted on 3 Jan 2021

HAL is a multi-disciplinary open access archive for the deposit and dissemination of scientific research documents, whether they are published or not. The documents may come from teaching and research institutions in France or abroad, or from public or private research centers.

L'archive ouverte pluridisciplinaire **HAL**, est destinée au dépôt et à la diffusion de documents scientifiques de niveau recherche, publiés ou non, émanant des établissements d'enseignement et de recherche français ou étrangers, des laboratoires publics ou privés.

Modeling the fretting fatigue endurance from partial to gross slip: the effect of debris layer

P. Arnaud, S. Fouvry

Ecole Centrale de Lyon, LTDS, Ecully, France

Corresponding author: siegfried.fouvry@ec-lyon.fr

Abstract

Fretting Fatigue (FF) appears as a key damaging process in many industrial assemblies subjected to vibrations. In this study, the “U-shape” experimental fretting fatigue endurance evolution of a 35NiCrMo16 steel cylinder/plane contact versus the applied displacement amplitudes is compared versus a complete finite element modeling. This latter takes into account the crack nucleation process, the crack propagation phenomena but also the surface wear as well as the evolution of the “third body” debris layer entrapped within the interface. This dynamical simulation of the fretting fatigue endurance from partial to gross slip condition confirms that surface wear effects can be neglected under partial slip (PS) but must be taken into account including the debris layer effect, in order to predict the fretting fatigue endurance under gross slip (GS) conditions. Using this (PS-NoWear/GS-Wear&ThirdBody) numerical framework, calibrated from a restricted set of plain fatigue experiments, an original “**DSN**” fretting fatigue chart strategy allowing a global description of the fretting fatigue damages (wear, crack nucleation and failure) as a function of **D**isplacement amplitude, fatigue **S**tress and **N** loading cycles is introduced and discussed.

Keywords: fretting fatigue; fretting wear; FEM simulation; lifetime prediction

1. Introduction

Most of the contacting assemblies subjected to vibrations and cyclic fatigue stressing are enduring fretting fatigue damage, like wear and cracking. These phenomena are considered as a plague in many industrial components like shafts or turbine engine dovetails (fig.1 a).

Waterhouse [1], Vincent [2] and Vingsbo [3], were the first to underline that the damage evolution depends on the sliding conditions. As long as the contact is running under partial slip (PS), the quasi linear rising of the tangential force with the displacement amplitudes, promotes an increase of the contact stressing and consequently a reduction of the fretting fatigue endurance. Alternatively, longer gross slip (GS) amplitudes, by favoring surface wear, decrease the contact peak pressures, the cyclic contact stressing and remove the incipient surface cracks. These combined effects reduce both crack nucleation and crack propagation promoting a successive rising of the fretting fatigue endurance.

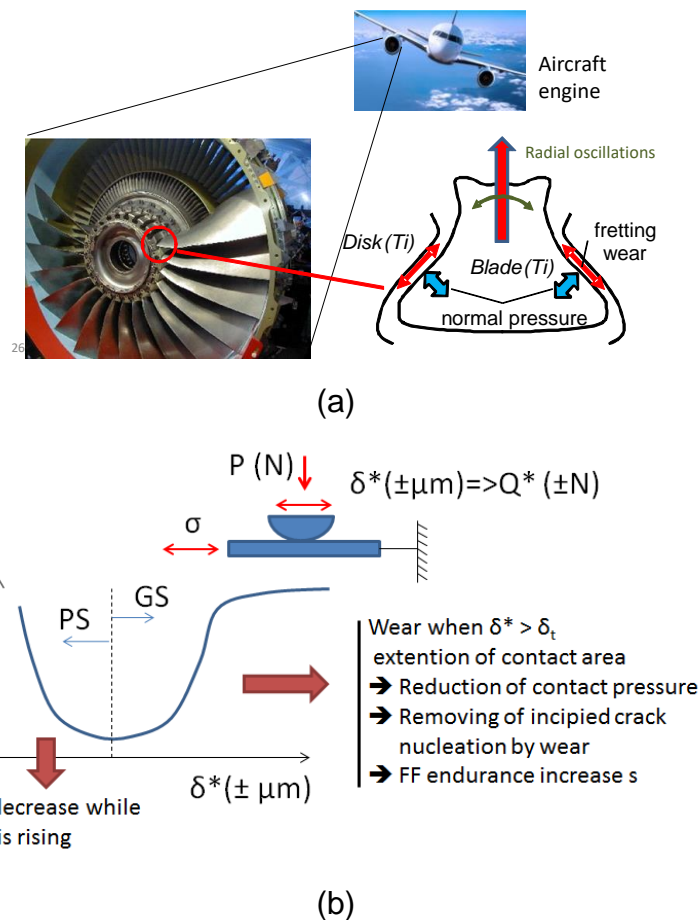


Fig. 1: a) illustration of fretting fatigue problem in aircraft engine; b) schematic evolution of fretting fatigue endurance (N_f) as a function of displacement amplitude (δ^*) (PS: partial slip, GS: gross slip, Q^* : tangential force amplitude).

Hence, a “U shape” non-monotonic fretting fatigue endurance evolution versus displacement amplitude is usually observed with a minimum value at the PS/GS transition when the maximum contact stressing is reached, whereas surface wear is not effective yet.

Modeling this “U shape” endurance curve is quite complex. It requires to simulate the crack nucleation rate considering the stress gradient induced by the contact [4-6]. It also implies to consider a short crack arrest description to predict crack propagation behavior [7, 8]. However, the most critical aspect concerns the combined simulations of wear and cracking phenomena under gross slip conditions [9-12]. An accumulated damage approach is indeed required to consider the stress evolution induced by the worn surface evolution. Besides, recent developments underline the necessity to consider the debris layer (i.e. third body) entrapped within the interface [13]. The latter modifies the contact pressure profiles and therefore the cracking process.

The purpose of this research work is to develop a global modeling strategy to predict the evolution of the fretting fatigue endurance as a function of displacement amplitude. First, fretting fatigue experiments will be performed to investigate the cylinder/plane fretting fatigue endurance of a well-known 35NiCrMo16 low alloyed steel. Using a double actuator test device [15], normal force and fatigue stressing were kept constant whereas the effect of displacement amplitude was investigated from partial to gross slip conditions. Then, a global FEM-python-matlab code was developed to simulate the experimental “U shape” fretting fatigue endurance curve. To calibrate the model, both crack nucleation law and fretting wear rate were extracted from a specific post processing analysis of plain fretting experiments. Various numerical strategies such as no wear (NW), wear without debris layer (W) and wear with debris layer (W&TB) hypothesis are compared versus experimental results. The influence of the debris layer is also discussed regarding crack nucleation and crack propagation responses.

1. Material and contact configuration

1.1. Material

The study focuses on a 35NiCrMo16 (investigated plane) / 52 100 (Cylinder) steel interface. 35NiCrMo16 is a high strength low alloyed steel extensively applied in

aeronautical industries. Cylinder pads are made of hard 52100 chromium steel to ensure that cracks initiate only in the 35NiCrMo16 specimens. The mechanical properties of the studied alloys are compiled in table 1.

Table 1: mechanical properties of studied steels.

	Elastic modulus, E (GPa)	Poisson coefficient, ν	Hard. HRC	Yield stress, $\sigma_{Y0.2\%}$ (MPa)	Ultimate stress σ_u (MPa)	fat. limit $\sigma_{D(-1)}$ (MPa)
52 100	195	0.3	62	1700		
35NCD16	205	0.3	37	950	1130	575

1.2. Contact configuration

A single contact configuration is applied either for fretting fatigue or plain fretting experiments. The 52 100 cylinder pad radius is set at $R=40$ mm and the normal load at $P=400$ N/mm inducing a $p_{max}=590$ MPa maximum Hertzian pressure and $a_H=0.43$ mm Hertzian contact radius (fig 2 a). The lateral width of the pad was set at $W=8$ mm to ensure 2D plain strain hypothesis. The contact remains under elastic conditions.

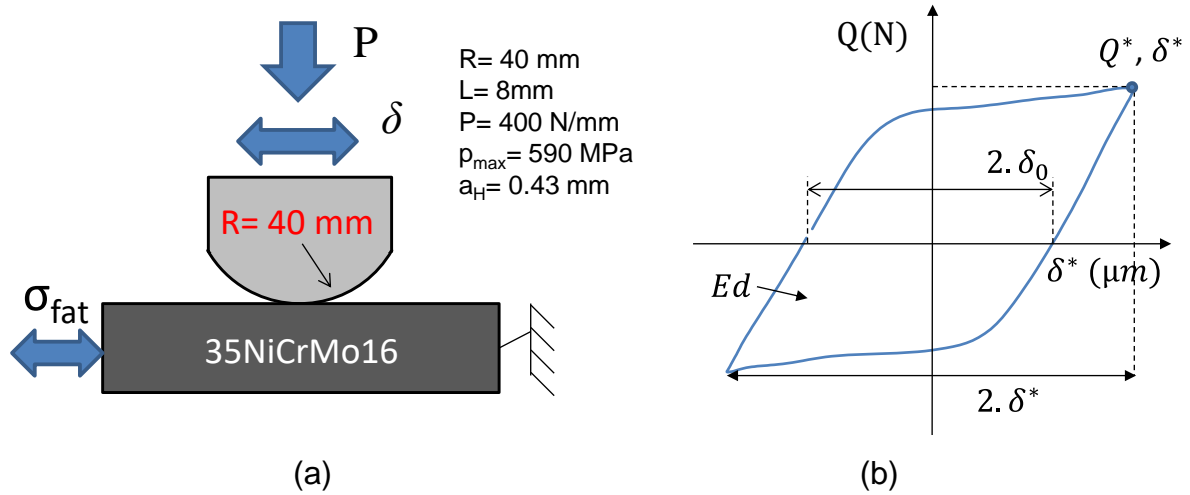


Fig. 2: a) studied contact configuration; b) fretting cycle (R : cylinder radius, L : lateral width, P : linear normal force, Q : tangential force, Ed : friction energy, δ^* : displacement amplitude, δ_0 : sliding amplitude established when $Q=0$).

The plotting of the fretting loop (i.e. the evolution of the tangential force versus the displacement) allows the determination of both Q^* tangential force and δ^* displacement amplitudes (Fig. 2b). It also provides the friction energy (Ed (J))

imputed in the interface (i.e. area of the fretting loop). Summing the friction work over the whole test duration provides the accumulated friction energy $\sum Ed$ (J) used to quantify the fretting wear rate [16,17]. To quantify the sliding condition, the friction energy criterion is applied [17]:

$$A = \frac{Ed}{4 \times \delta^* \times Q^*} \quad (1)$$

Former investigations suggest that the contact is running under partial slip if $A < At = 0.2$ and under gross slip if $A > At$.

All the tests done under partial slip condition were performed at 5 Hz. However, to prevent adhesive wear processes (i.e. metal transfers and seizure), the frequency was then decreased to 0.5 Hz under gross slip condition [18]. Fatigue cracking process is assumed independent of frequency at least for the studied 0.5 – 5hz conditions.

1.3. Fretting fatigue experiments

The fretting fatigue experiments were performed using a double actuator fretting fatigue test system previously detailed in [19]. The principle of this test machine, introduced by Oxford group [15], consists in a bottom hydraulic actuator imposing the fatigue stress and a top hydraulic actuator inducing the pad fretting displacement (fig. 3 a). Again, the normal force P is maintained constant using a trolley assembly.

Note that the given investigation focuses on the fretting fatigue endurance versus displacement amplitude. Measuring contact displacement under fretting fatigue condition is quite complex because it requires to consider the relative displacement at the contact point of the fatigue specimen which is also moving due to the cyclic fatigue strain. To control this perturbation, tests were performed using a phase fretting and fatigue displacement configuration (Fig. 3). This implies that both fretting pad and the fatigue strain are in phase following the same direction. As mentioned, the fatigue stress was maintained constant ($\sigma_{max} = 400$ MPa, $\sigma_{min} = 40$ MPa, $R_\sigma = 0.1$).

If no displacement is imposed to the pad, a residual tangential force is generated in the contact due to strain deformation of the fatigue specimen. When a Δ^* displacement amplitude is imposed to the pad using the top actuator, the relative displacement at the contact point is first decreased inducing a reduction of the fretting tangential force. The tangential force amplitude decreases until a minimum value

near zero when $\Delta^* = \Delta^*_0$ which corresponds to the situation where the pad displacement is fully accommodating the fatigue strain displacement at the contact position. Increasing the top actuator displacement, the tangential force rises again until a plateau when the gross slip condition is reached. Hence in the following analysis, the fretting contact displacement amplitude (δ^*) will be expressed as a function of the pad displacement so that:

$$\delta^* = \Delta^* - \Delta^*_0 \tag{2}$$

Whereas the fretting sliding amplitude is given by

$$\delta_0 = \delta^* - \delta_t \tag{3}$$

with δ_t the fretting displacement marking the gross slip transition (i.e. onset of the tangential force plateau).

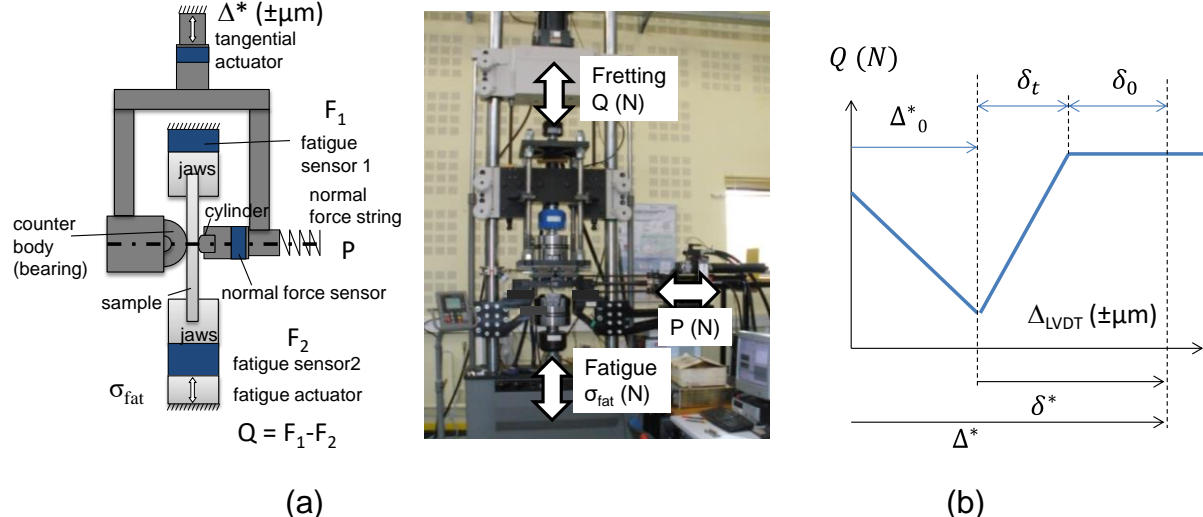


Fig. 3: a) illustration of the fretting fatigue test machine; b) illustration of the in phase fretting fatigue test procedure.

The test were stopped at failure or at 10^6 cycles which implies a test duration of more than 23 days with $f = 0.5$ Hz. Figure 4 compares the evolution of the fretting fatigue endurance versus the displacement amplitude δ^* .

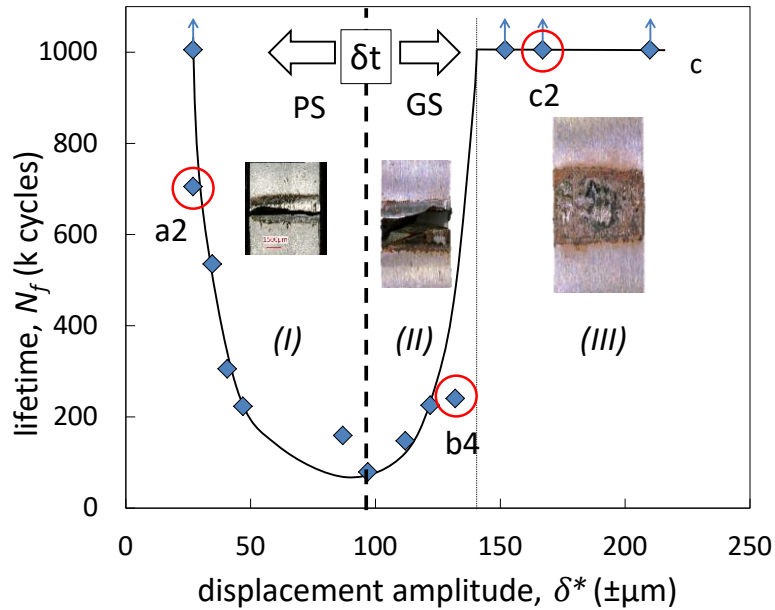


Fig. 4: Experimental fretting fatigue lifetime as a function of fretting displacement amplitude (35NCD16/52100), $R=40$ mm, $P=400$ N/mm, $\sigma_{fat}=400$ MPa, $R_{fat}=0.1$, $f=5$ Hz in partial slip and 0.5 Hz in gross slip (a2 : $\delta^*=\pm 25$ μm ; b4: $\delta^*=\pm 130$ μm ; c2 : $\delta^*=\pm 165$ μm).

As expected, the global tendency of the fretting fatigue endurance is non-monotonic. Three domains can be considered. The first domain I, is related to partial slip condition displaying a continuous reduction of the fretting fatigue endurance until minimum value at the partial slip/gross slip transition. Then, above $\delta_t \approx 97 \mu\text{m}$, the lifetime rises again due to surface wear and related contact stress reduction. Surface observation at the contact opening reveals a significant contact area extension and a chaotic crack path (domain II). Finally, for the longest displacement amplitudes, the samples do not fail after 10^6 cycles, so that the fretting fatigue endurance is assumed infinite (domain III). The analysis of the coefficient of friction from the partial slip/gross slip transition to the gross slip regime reveals a quasi-constant value around 0.75 ± 0.05 . Surface and cross section observations but also 3D surface profiles were performed to characterize the various fretting fatigue damage generated as a function of the displacement amplitude (Fig. 5).

3D surface profile of partial slip fretting fatigue test a4 (domain I) shows no surface wear. A straight crack is observed inside the fretted surface despite the fact it should be nucleated at the contact border where the maximum tensile stressing is operating.

This shift may be explained by a small contact area extension induced by a drop of the normal contact stiffness with the fretting fatigue crack extension. This was demonstrated by M.C. Dubourg et al. [20] who observing the fretting cracking of PMMA transparent material, concluded that first cracks are well nucleated at the contact borders, but due to the crack extension, the contact stiffness decreases and the fretted area extended so that at the end of the fretting test, cracks appear inside the fretted area. Fracture surface observation underlines rather straight crack path suggesting a dominant mode I influence.

Fretting Fatigue scars generated in gross slip domain II (test b4) (Fig. 4 & 5b) are characterized by a significant surface wear extension and a disturbed crack path located in the middle of the fretting scar. The lateral contact radius if multiplied by a factor 3 compared to the Hertzian hypothesis and the maximum wear depth reaches 25 μm . Cross section observations show an initial slant crack followed by a straight crack extension when the crack exits from contact stress influence.

The expertise of the domain III gross slip infinite life time (test c1) (Fig. 4 & 5c) confirms a huge surface wear extension. Deep “U-shape” fretting scars are observed showing a contact radius extended up to 2.65 mm (more than 6 time the contact radius) and a maximum wear depth around 60 μm . Surface observations as well as cross section expertise do not reveal any surface crack nucleation longer than 10 μm . This suggests that for such long sliding amplitudes, the surface wear process is fast enough to prevent any cracking phenomenon.

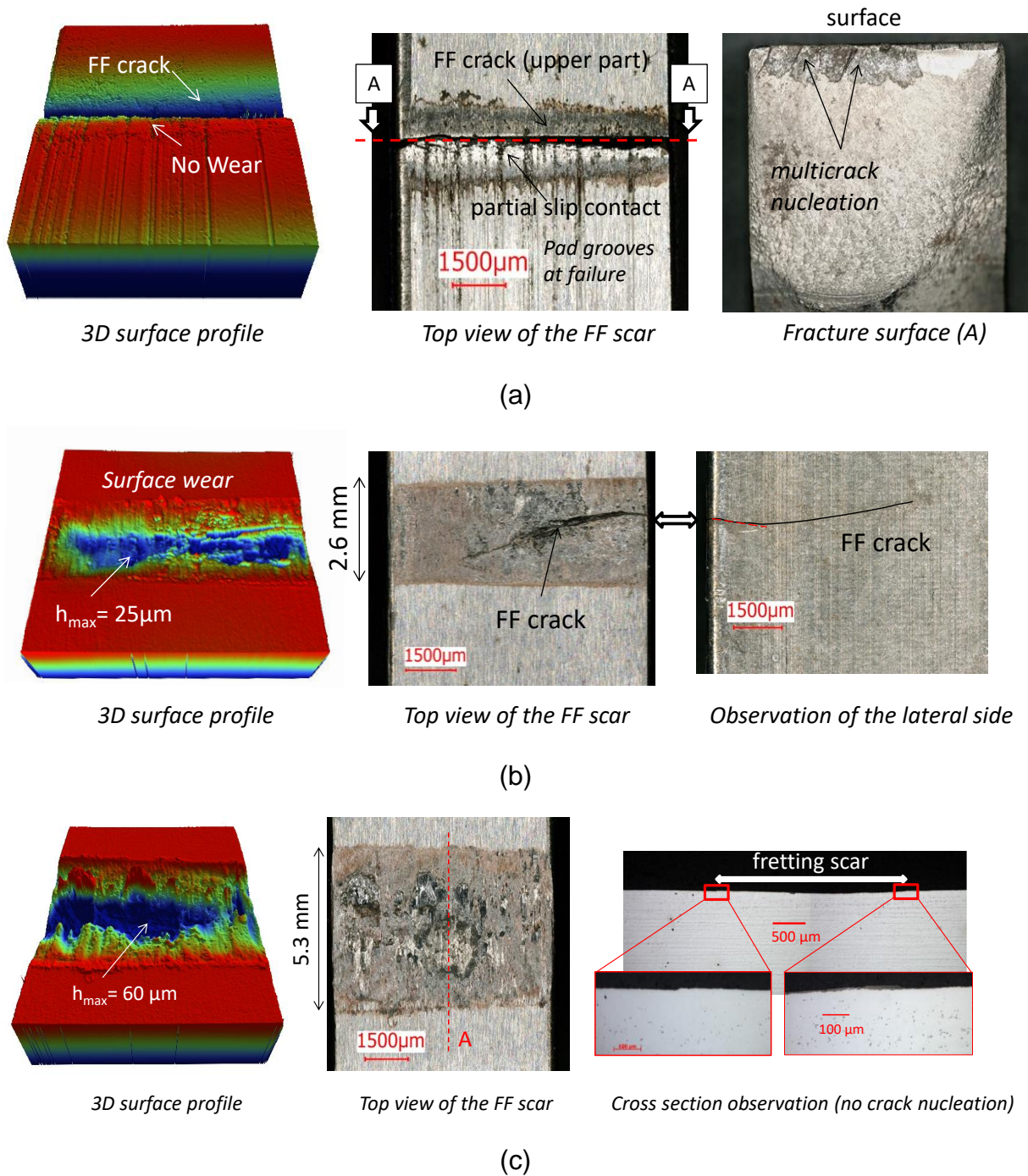


Fig. 5 : Expertise of 3 representative Fretting Fatigue (FF) scars including 3D surface profile, optical top view and crack observation (test reference given in Fig. 4): (a) test a2 (partial slip domain I) ; (b) test b4 (gross slip domain II); (c) test b4 (gross slip domain III).

2. Modeling

The chosen modeling strategy consists in computing the fretting fatigue cycles in order to predict the failure N_f as a function of the applied displacement amplitude δ^* so that:

$$N_f = N_N + N_p \quad (4)$$

Where N_N is the number of fretting fatigue cycles inducing the nucleation of a 10 μm crack length whereas N_p concerns the fretting fatigue cycles inducing the propagation until failure. The model is elastic and can also consider the debris layer entrapped within the interface. Wear is neglected under partial slip condition.

2.1. FE Model

An Abaqus FE Model was developed to reproduce the experiments as close as possible. A 2D plain strain cylinder/plane contact was meshed (Fig. 6). The friction response is simulated using a coulombian friction law with $\mu=0.75$. The back contact behind the fatigue specimen is simulated using a ball bearing applying a similar normal load but without tangential force (i.e. no friction coefficient). A so called “fretting box”, where both surface wear and cracking processes are simulated, is implemented in the fatigue specimen next to the contact zone. It consists in a fine 20 μm quad meshing. Applying a $P=400 \text{ N/mm}$ normal load, it implies at least 42 contacted elements for the initial unworn interface which is barely sufficient to describe pressure and shear surface profiles. A second part below the “fretting box” is designed to compute the crack propagation. Four reference points (RF) are used to define the boundary conditions and apply the loading sequences of the model (Fig. 6a). The reference point (RF1) drives the cylinder applying the fretting loading (normal force and tangential displacement). The second reference point (RF2) applies a similar tangential displacement without friction and a opposite normal force to the ball bearing to avoid any bending effect on the fatigue specimen. Reference point 3 (RF3) fixes the fatigue sample whereas RF4 drives the fatigue stress. The finite elements computation is divided in 3 steps (Fig.6 c). The first one consists in applying mean fatigue stress to the fatigue sample and to move the cylinder and the bearing in order to keep the contact in the middle of the “fretting box”. The second one applies the normal load on cylinder and bearing. Finally, the last step simulates the fretting fatigue cycles. A periodic displacement amplitude is imposed on RF1 and RF2 in phase with the RF4 fatigue loading as imposed in the experiments.

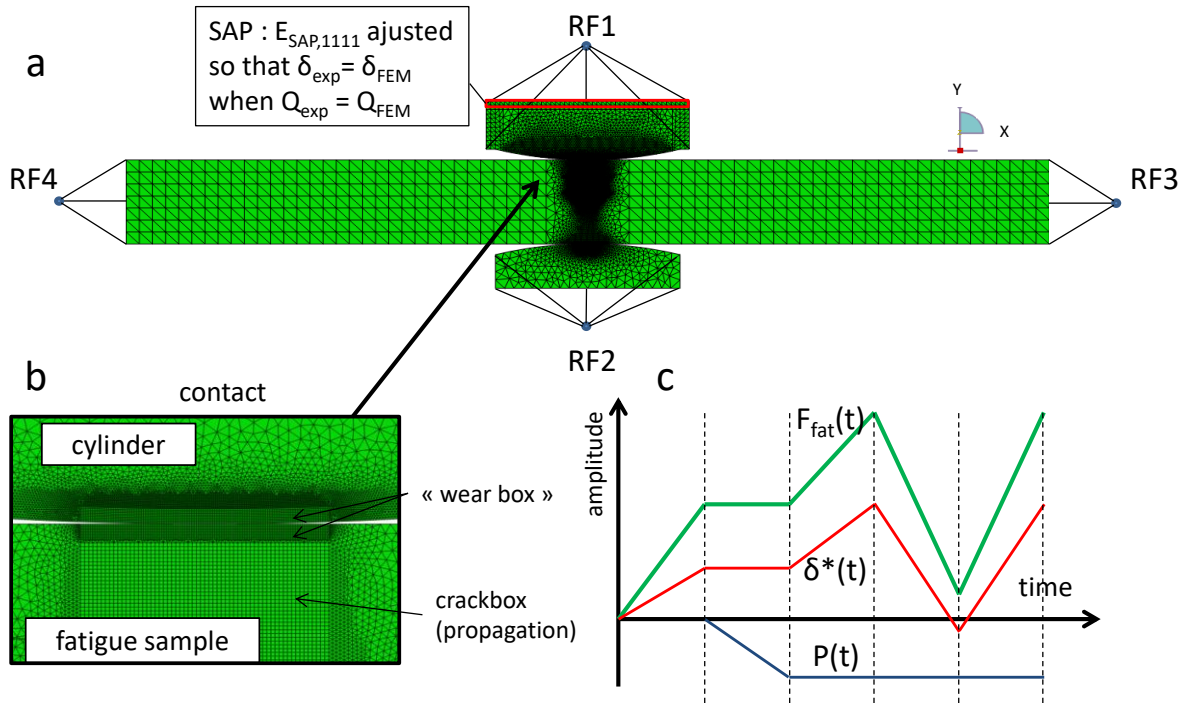


Fig. 6: FE model used for fretting fatigue simulations; (a) Full model; (b) mesh at contact interface; (c) loadings applied to the model.

The given analysis consists in comparing the fretting fatigue damage as a function of the displacement amplitude. Hence, there is a critical interest to establish a correlation between the experimental and simulated displacement amplitude δ^* . This was done using a former methodology developed in [12]. An additional System Accommodation Part (SAP) is added at the top of the cylinder whose $E_{SAP2,1111}$, orthotropic elastic property is adjusted until the simulated transition amplitude corresponds to the experimental value:

$$\delta_{t,FEM} = \delta_{t,exp} \quad (5)$$

Hence, using this “SAP” concept a direct correlation between experimental and simulated δ^* displacement amplitudes can be established.

2.2. Crack nucleation law

2.2.1. Numerical implementation

The crack nucleation analysis is performed by applying the SWT multiaxial fatigue stress criterion [21]. It is defined as the maximum value of the product of the maximal normal stress and the normal strain amplitude applied to the θ material plane [22].

This analysis is performed each the M position of the integration point of the “fretting box” part (Fig. 7).

$$\Gamma(M, \theta) = \sigma_{max}(\theta, M) \times \frac{\Delta\varepsilon(\theta, M)}{2} \quad (6)$$

With

$$\sigma_{max}(\theta, M) = \max_t[\sigma(t, \theta, M)] \quad (7)$$

$$\Delta\varepsilon(\theta, M) = \max_t[\varepsilon(t, \theta, M)] - \min_t[\varepsilon(t, \theta, M)]$$

Considering a $20\mu\text{m}$ mesh size, this implies a distance between the top surface and the first layer of integration points equals to $L_{ip}=10\mu\text{m}$.

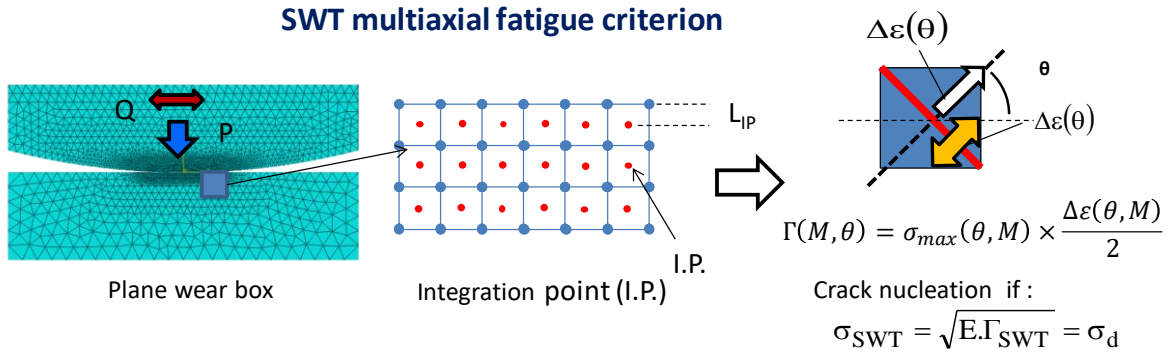


Fig. 7: Illustration of the computation of the SWT parameter.

Surface wear by modifying pressure and shear stress profiles induces an evolution of the SWT criterion. Hence, an accumulated damage approach is required to predict the cracking risk. A linear Palmgren-Miner rule is here considered so that for each integration point and for each i^{th} numerical step, an increment of damage $\Delta D_{(i)}^{IP}$ is computed:

$$\Delta D_{(i)}^{IP} = \frac{\beta_{(i)}}{N_{N,(i)}^{IP}} \quad (8)$$

With $\beta_{(i)}$ the numerical jump also related to the number of real fretting cycles simulated during each i^{th} numerical increment and $N_{N,(i)}^{PI}$ the related number of fretting cycle inducing crack nucleation for the corresponding $\Gamma_{(i)}^{IP}(M, \theta)$ value. Then for each integration point (IP), the cumulated damage is computed summing the contribution of each numerical integrations. Due to the worn profile evolution, a damage transfer field strategy is also adopted to transfer the former $(i-1)^{\text{th}}$ damage value to the next i^{th} IP position using a basic linear field transfer (FT) interpolation, so that:

$$D_{(i)}^{IP} = \Delta D_{(i)}^{IP} + FT_{(i)}(D_{(i-1)}^{PI}) \quad (9)$$

Crack nucleation is assumed when the maximum value of $D_{(i)}^{IP}$ found in the “fretting box” is becoming larger than 1:

$$\text{Crack nucleation if } D_{max} = \max_{IP} (D_{(i)}^{PI}) \geq 1 \quad (10)$$

2.2.2. Identification of the crack nucleation law

A key issue of the model concerns the identification of the crack nucleation law, $N_n = g(\Gamma)$. For conventional fatigue problems, this endurance response can be extrapolated from fatigue data. However, for the studied alloy these data were not available. Besides, fretting fatigue stressing is characterized by very sharp stress gradients which imply non-local fatigue stress analysis [5-6]. A post processing strategy consisting in identifying the crack nucleation endurance from plain fretting experiments is here adopted [5,12, 23]. This strategy, previously developed for infinite lifetime conditions, is presently extended to finite endurance conditions (Fig. 8). It consists in performing partial slip plain fretting tests (i.e. without fatigue stress) for different fretting cycles using similar cylinder/plane contact geometry. After each test, cross section observations are performed along the median axis of the fretting scar. Then, the projected maximum crack lengths are plotted as a function of the applied tangential force amplitude. Plain fretting experiments are less expensive, given that 3 tests may be performed and simultaneously cross-sectioned and expertised using small $20 \times 20 \times 15$ mm square specimen. However, because no fatigue stress is imposed, higher pressure and shear fretting stressing must be applied to simulate similar cracking process. Using an explicit formulation of the stress state at the trailing contact border [23], it was found that equivalent fretting fatigue cyclic stresses can be reached if the normal force is raised up to $P=1000$ N/mm. To avoid the short crack arrest complexity, the strategy consists in identifying the crack nucleation for a crack length equivalent to the transition from short to long crack propagation regime assuming the Kitagawa approximation [7]:

$$b_0 = \frac{1}{\pi} \left(\frac{\Delta k_0}{\sigma_D} \right)^2 \quad (11)$$

For the studied alloy, we found $b_N=b_0= 10 \mu\text{m}$.

Figure 8a compares the evolutions of the maximum projected crack length as a function of the applied tangential force for different test durations. The corresponding crack nucleation tangential forces Q_N^* related to $b_N= 10 \mu\text{m}$ crack length are identified,

compiled and plotted in figure 8b. As expected, an asymptotic decreasing power law function is established converging to the threshold fatigue limit established at 10^6 cycles. This implies the following relationship:

$$\begin{aligned} N < 10^6 : Q_N^* &= Q_0^* \times N^{n_0} \\ N > 10^6 : Q_N^* &= Q_N^*(10^6) \end{aligned} \quad (12)$$

For the studied condition, it was found $Q_0^*=1720$, $n_0= -0.124$ and $Q_N^*(10^6) = 310$ N/mm. To capture the stress gradient effect, the critical distance method is adopted [5,6]. It consists in performing the fatigue stress analysis not at the surface hot spot (HS) but at a “critical distance” l below this latter (Fig. 8c). A useful strategy to identify a pertinent critical distance consists in applying a post processing analysis of the 10^6 cycles partial slip plain fretting crack nucleation condition [23]. On the other hand the l value must be adjusted until to solve the following relationship:

$$\sigma_{SWT}(x = -a_H, z = l) = \sigma_D \quad (13)$$

Where $\sigma_D=575$ MPa [23] is the alternated tensile fatigue limit of the studied alloy and σ_{SWT} is the corresponding equivalent SWT stress where:

$$\sigma_{SWT} = \sqrt{E \times \max_{\theta} \Gamma(x, z, \theta)} \quad (14)$$

Applying a basic iterative analysis for the $Q_N^*(10^6)$ crack nucleation, it was found a critical distance value about $l= 30 \mu\text{m}$ (Fig. 8c). This value is assumed constant (i.e. nondependent of the test duration) which allow us to plot the corresponding SWT crack nucleation endurance curve (Fig 8d).

By fitting the given crack nucleation endurance curve, and assuming a flat evolution above 10^6 cycles it leads to the following relationships:

$$\begin{aligned} \text{if } N < 10^6 : \Gamma_N &= \Gamma_N(z = l, Q_N^*) = \Gamma_0 \times N^{n_p} \\ \text{if } N > 10^6 : \Gamma_N &= \Gamma_N(z = l, Q_{10^6}^*) = \Gamma_{N,\infty} \end{aligned} \quad (15)$$

For the studied 35NcNiMo16 alloy, fretting conditions and $b_N=10 \mu\text{m}$ it was found $\Gamma_0=17.3$, $n_p=-0.19$ and $\Gamma_{N,\infty}=1.2$.

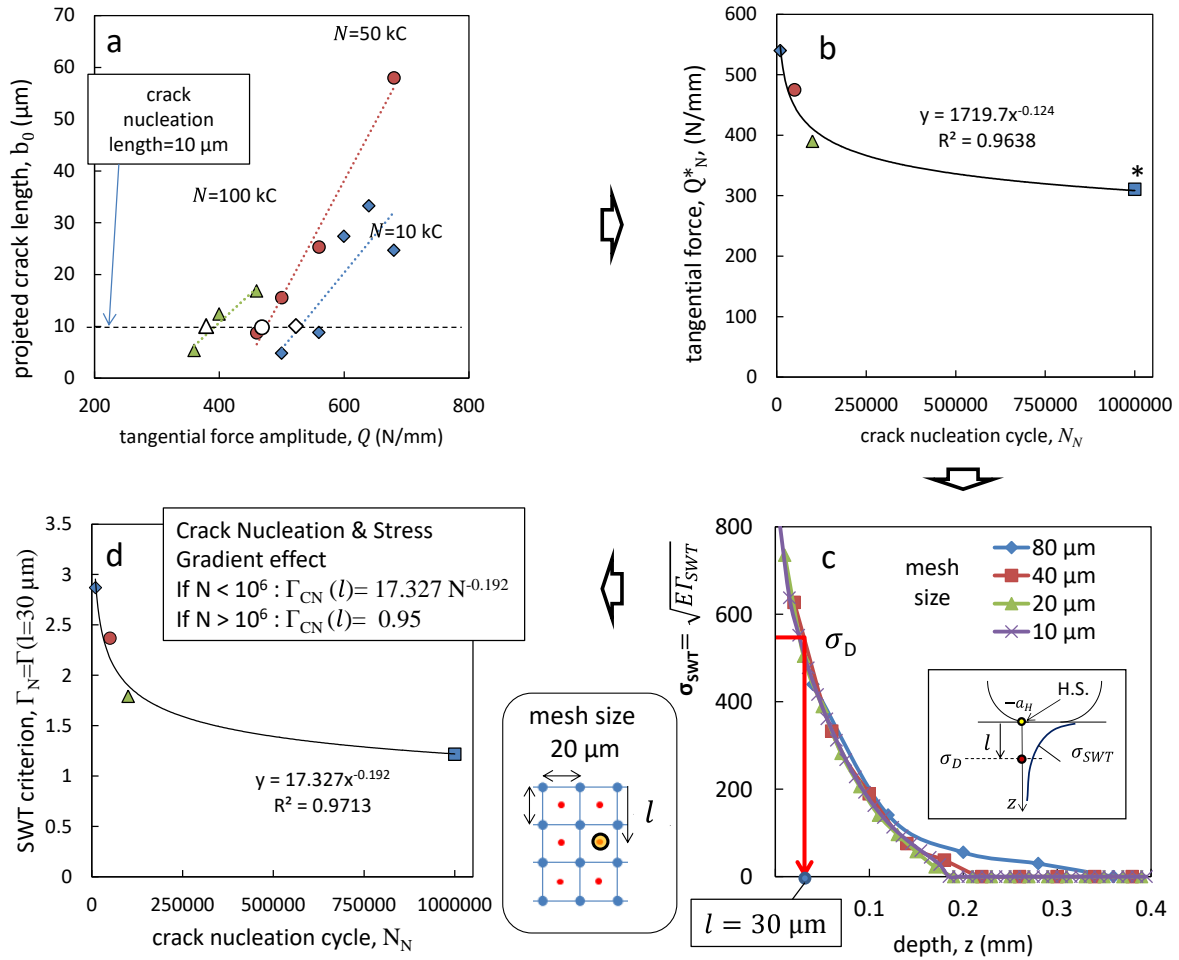


Fig. 8: Illustration of the post processing analysis of plain fretting test to identify the SWT crack nucleation law; a) experimental identification of threshold tangential force amplitude inducing crack nucleation ($b_N=10 \mu\text{m}$, $R=40 \text{ mm}$, $P=1000 \text{ N/mm}$); b) plotting of Q_N^* ($b_N=10 \mu\text{m}$) crack nucleation endurance curve; *[26]; c) identification of critical distance (l) where $\sigma_{swt} = \sigma_D$; d) identification of the corresponding SWT crack nucleation law (10^6 cycles) at the critical distance $l=30 \mu\text{m}$ below the Host Spot (HS).

2.3. Crack propagation law

A decoupled weight function is considered to extrapolate the stress intensity factors (SIF) at the crack tip. First, the σ_{11} stress field along a vertical axis at the trailing contact border is extracted at the maximum ($+Q^*$, σ_{max}) and minimum ($-Q^*$, σ_{min}) loadings. Then, the mode I stress intensity factor K_I is computed using the Bueckner weight function approach [24]:

$$K_I = \sqrt{\frac{2}{\pi}} \int_0^h M(t) \times \sigma_{11}(t) d(t) \quad (16)$$

with

$$M(t) = t^{-1/2} \left[1 + m_1 \times \frac{t}{h} + m_2 \times \left(\frac{t}{h} \right)^2 \right] \quad (17)$$

and

$$m_i = A_i + B_i r^2 + C_i r^6, \quad r = \frac{h}{w} \quad (18)$$

With $A_1 = A_{ref} = 0.6147$, $B_1 = 27.9558 \times A_{ref}$, $C_1 = 14.2870 \times A_{ref}$, $B_2 = 27.9558 \times A_{ref}$, $A_2 = 0.4070 \times A_{ref}$, $B_2 = 5.3504 \times A_{ref}$, $C_2 = 113.9489 \times A_{ref}$.

As suggested by various authors [22, 25] the effective SIF value can be approximated considering the single mode I contribution (i.e. K_I). Indeed, the compressive stresses imposed the normal loading but also the high friction coefficient operating within the crack lips tend to reduce the mode II contribution. The varying stress ratio below the contact is captured using the $R_K = K_{I,min}/K_{I,max}$ parameter [26] and combined with the effective Kujawski fatigue crack driving force parameter to formalize the crack propagation rate [27].

$$\bar{K}^* = (\Delta K^+)^{0.5} \times K_{I,max}^{0.5} \quad (19)$$

With $\Delta K^+ = K_{I,max} - K_{I,max}$ for $R_K > 0$ and $\Delta K^+ = K_{I,max}$ for $R_K \leq 0$. Note that, using this formulation, both ΔK^+ and \bar{K}^* are systematically higher or equal to zero.

The propagation endurance N_p is finally estimated by coupling the Kujawski's fatigue-crack-driving force parameter and the Paris's law solving the following integral:

$$N_p = \int_{b=b_N}^{b_{failure}} \frac{db}{C \bar{K}^{*m}} \quad (20)$$

The Paris law parameters are extracted from literature [28]. For the studied 35NiCrMo16 alloy it was found $C=3.366 \cdot 10^{-8}$, $m=2.5$, $\Delta K_0=3.2 \text{ MPa}\cdot\text{m}^{-0.5}$, $K_{IC} = 300 \text{ MPa}\cdot\text{m}^{-0.5}$. Note that only long crack regime is considered according that $b_N = b_0$. Crack arrest and failure conditions are therefore expressed by the following relationships:

$$\text{If } \bar{K}^*(b) \leq \Delta K_0 \text{ then crack arrest condition } (N_p \text{ tends to infinite}) \quad (21)$$

$$\text{If } K_{I,max} \geq K_{IC}, \text{ the failure condition is reached.} \quad (22)$$

2.4. Wear simulation with debris layer consideration

Wear modeling

Wear volume generated on plane and cylinder surfaces are expressed as a linear function of the accumulated friction energy imputed in the interface ($\sum Ed$).

$$V_p = \alpha_p \times \frac{\sum Ed}{2} \quad \text{and} \quad V_c = \alpha_c \times \frac{\sum Ed}{2} \quad (23)$$

Where α_p and α_c are the energy wear coefficients related to plane and cylinder respectively. The FEA surface wear modeling consists in transposing the global wear volume approach to a local wear depth simulation [13, 29, 30]. After each i^{th} fretting cycle, the $\varphi_i(x)$ friction energy density profile is computed. The related wear depth increments are expressed according that:

$$\Delta h_{p,(i)}(X) = \beta_{(i)} \times \alpha_p \times \frac{\varphi_i(x)}{2} \quad (24)$$

and

$$\Delta h_{c,(i)}(X) = \beta_{(i)} \times \alpha_c \times \frac{\varphi_i(x)}{2} \quad (25)$$

Where $\varphi_i(x)$ is the friction energy density imputed at the x position during the i^{th} fretting cycle, and $\beta_{(i)}$ the numerical jump allowing to simulate β experimental cycles during each i^{th} numerical cycle. The value of $\beta_{(i)}$ is calculated to achieve a maximum wear depth increment of $0.1 \mu\text{m}$ thus to avoid any numerical distortion on pressure profiles. This surface wear modeling is implemented in the matlab-python abaqus fretting box. Surface wear evolution is simulated on both cylinder and plane counterparts applying a node translation procedure as illustrated in figure 9. A full detail of the procedure is given in [12].

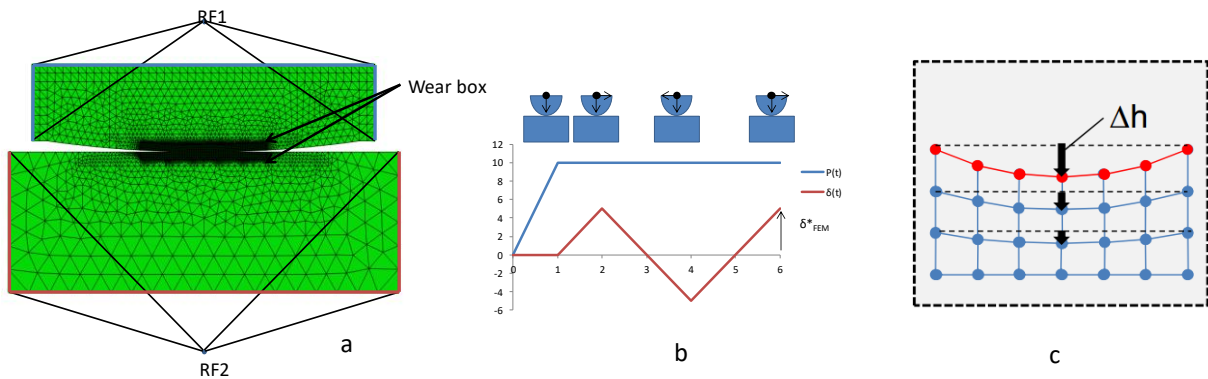


Fig. 9: illustration of the numerical procedure used to simulate surface wear evolution after [12]. a) FEM model (plain fretting); b) fretting loading sequence, c) surface and subsurface node procedure used to simulate the surface wear profile evolution.

Third body modeling

The main idea to simulate the third body debris layer consists in inserting between the two counterparts a debris layer. The principle of the model is illustrated in figure 9 and fully detailed in [14].

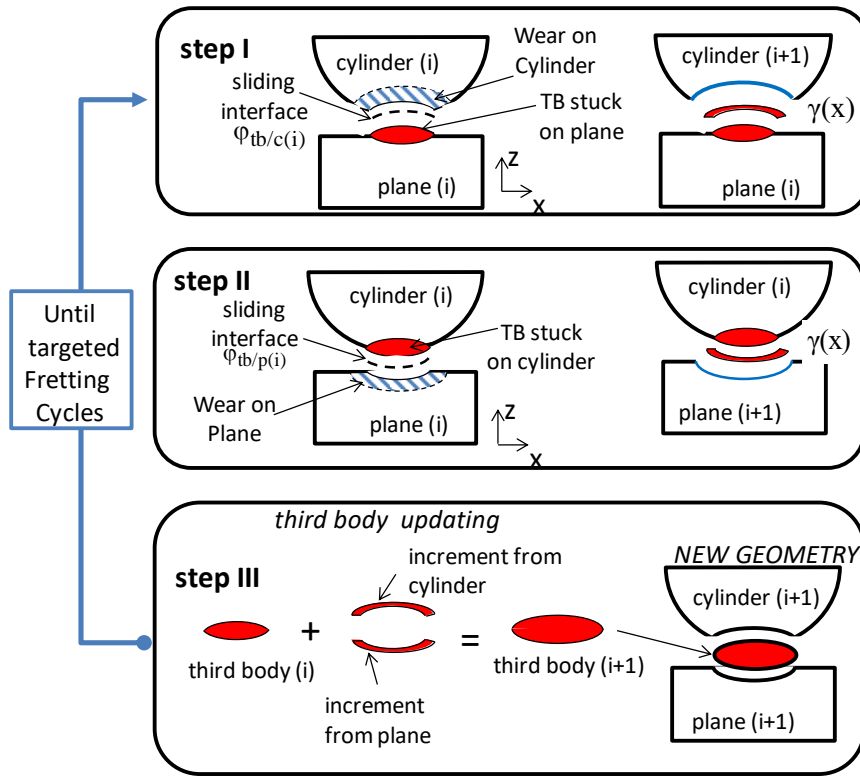


Fig. 10: Illustration of the algorithm used to simulate the surface wear of plane and cylinder counterpart taking into account a dynamical third body layer.

The model involves two sliding interfaces: a first one between the cylinder and the debris layer stuck on the plane so called “dc” interface and a second one between the plane and the debris layer now stuck on the cylinder so called “dp” interface. These two sliding interfaces cannot be simulated simultaneously. A first step of the numerical cycle consists in computing the $\varphi_{dc,(i)}(x)$ friction energy profile between the “dc” interface then the $\varphi_{dp,(i)}(x)$ profile related to the “dp” interface.

Assuming an equipartition of friction dissipation, the increment of wear depths reported on cylinder and plane cylinder surfaces are established by substituting both $\varphi_{dc,(i)}(x)$ and $\varphi_{dp,(i)}(x)$ friction density profiles in equation 22 and 23. A second aspect of the model consists in monitoring the evolution of the debris layer FEM part by considering a $\gamma(x)$ third body conversion factor expressing the proportion of worn

thickness of plane and cylinder which are transferred toward the debris layer. The complement $1 - \gamma(x)$ is assumed eliminated (i.e. ejected) from the interface.

The i^{th} increment of debris layer added to the third body at the x position is therefore expressed by:

$$\Delta d_{(i)}(x) = \gamma_{(i)}(x) \times (h_{c,(i)}(x) + h_{p,(i)}(x)) \quad (26)$$

At the end of the numerical cycle both worn surfaces and third body layer are updated so that:

$$h_{p,(i)}(x) = h_{p,(i-1)}(x) + \Delta h_{p,(i)}(x) \quad (27)$$

$$h_{c,(i)}(x) = h_{c,(i-1)}(x) + \Delta h_{c,(i)}(x) \quad (28)$$

and

$$d_{(i)}(x) = d_{(i-1)}(x) + \Delta d_{(i)}(x) \quad (29)$$

A key aspect of the model concerns the expression of the $\gamma_{(i)}(x)$ function. Former investigations suggested that $\gamma(x)$ is not constant over the whole fretted interface but depends on the x longitudinal position. Indeed, considering the third body theory it can be assumed that $\gamma(x)$ is higher in the middle of the contact where debris are more easily captured in the debris layer than on the lateral sides where debris are more easily ejected from the interface. To illustrate such effect a simple parabolic formulation is considered:

$$\gamma_{(i)}(x) = -K_{\gamma(i)}x^2 + \gamma_{0(i)} \quad (30)$$

With $K_{\gamma(i)}$ and $\gamma_{0(i)}$ are depending on the wear volume extension and therefore may be expressed as a function of the accumulated friction energy.

Calibration of the wear model

The model implies to determine both α_p and α_c energy wear rates (Fig. 11) but also the two K_{γ} and γ_0 third body parameters. To identify these variables, few plain fretting wear tests were performed keeping constant the loading load: $P=400$ N/mm, $f=0.5$ Hz, $R=40$ mm and test duration $N=10^5$ cycles but varying the sliding amplitude δ_0 .

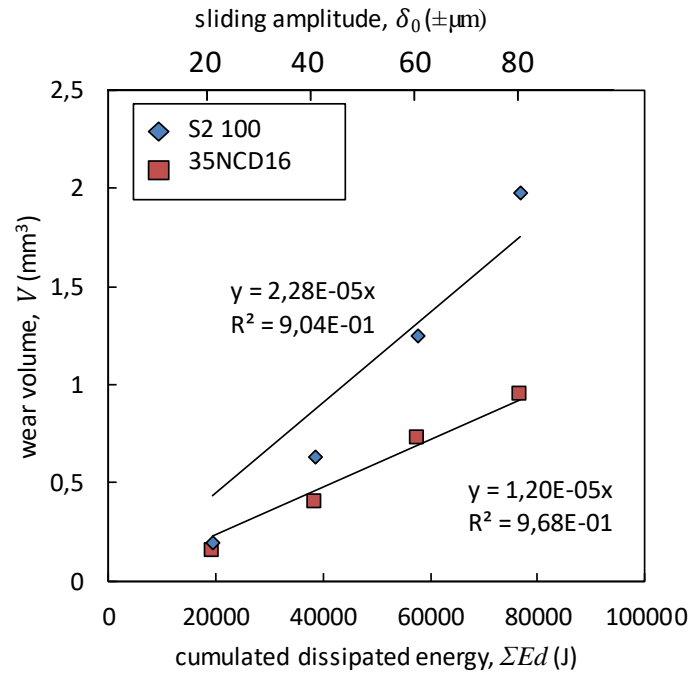


Fig. 11: Wear volume as a function of cumulated dissipated energy and sliding amplitude for cylinder and plane.

From these experiments both plane and cylinder wear rates were estimated respectively at $\alpha_p = 1.2 \cdot 10^{-5} \text{ mm}^3/\text{J}$ and $\alpha_c = 2.28 \cdot 10^{-5} \text{ mm}^3/\text{J}$. It is surprising to see that the harder 52100 steel displays a higher wear rate than the studied 35NiCrMo16 steel. This could be explained assuming a “basin” effect on plane which better maintains the debris layer on plane surface than on cylinder and therefore better protects the plane surface.

Both γ_0 and K_γ parameters are extrapolated from the fitting of the parabolic law (Eq. 30) with the experimental plotting of the $\gamma(x)$ function so that (Fig. 12):

$$\gamma(x) = \frac{h(x)}{d(x)} \quad (31)$$

with $h(x)$ the total worn profiles (i.e. $h(x) = h_c(x) + h_p(x)$) and $d(x)$ the inner gap measured between the two worn profiles when they are contacted on their lateral sides. This strategy was applied for various fretting wear conditions thus to extract the evolution of γ_0 and K_γ parameters as a function of the sliding amplitude, wear volume and related accumulated friction energy (Fig. 13a).

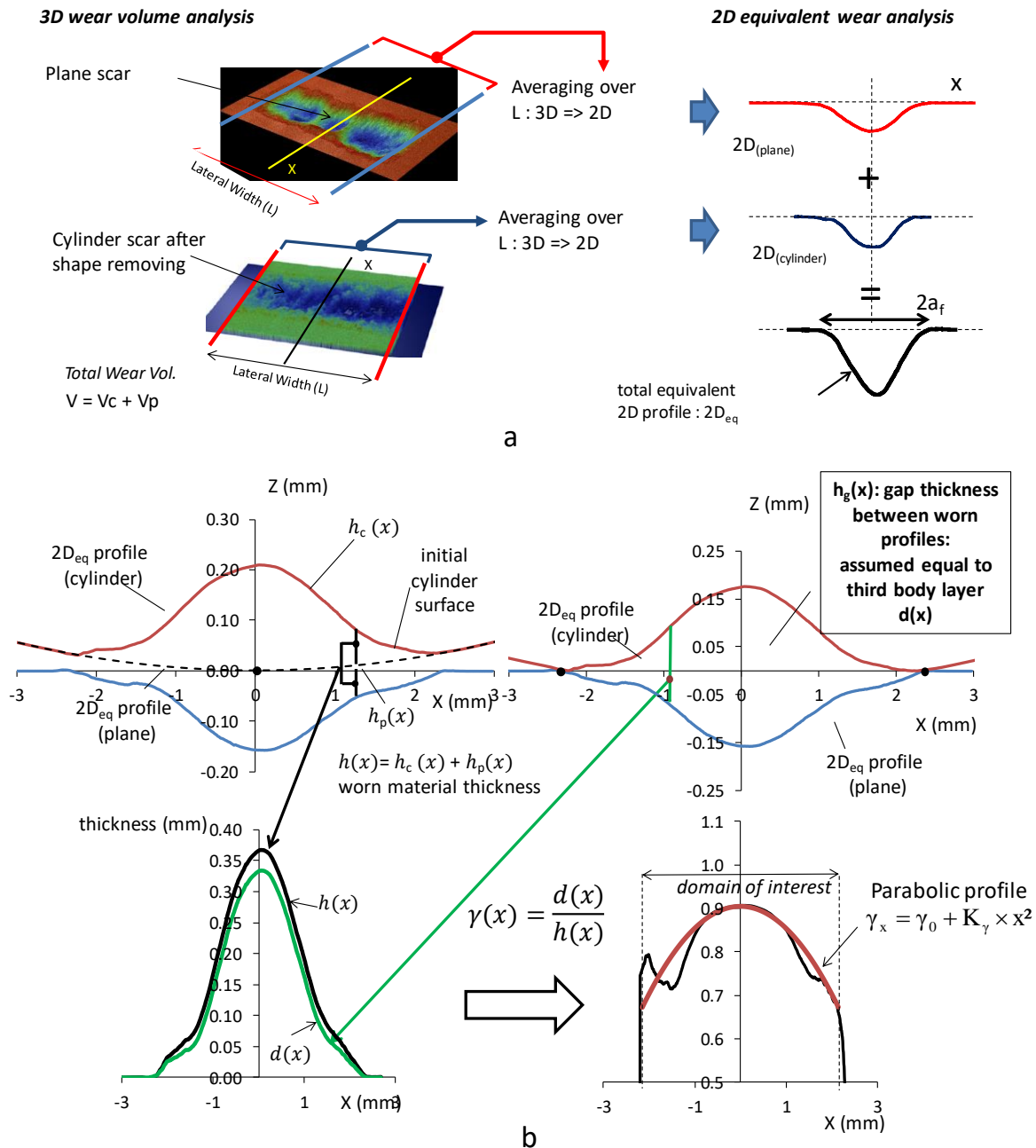


Fig. 12: illustration of methodology applied to quantify the fretting scar (after ultrasonic cleaning) ; a) averaging strategy used to extract representative 2D equivalent wear profiles from 3D surface analysis (b) determination of wear thickness profile ($h(x)$) and debris thickness profile ($d(x)$) by comparing both plane and cylinder worn 2D eq surface profiles.

The decreasing trends of both γ_0 and K_γ parameters is consistent with the third body theory. Indeed, extending the Godet's and Berthier's third body theory [31], Fillot et al. [32] demonstrated that the third body (i.e. debris layer) thickness reaches a steady state value when the debris ejection flow equals the debris formation rate.

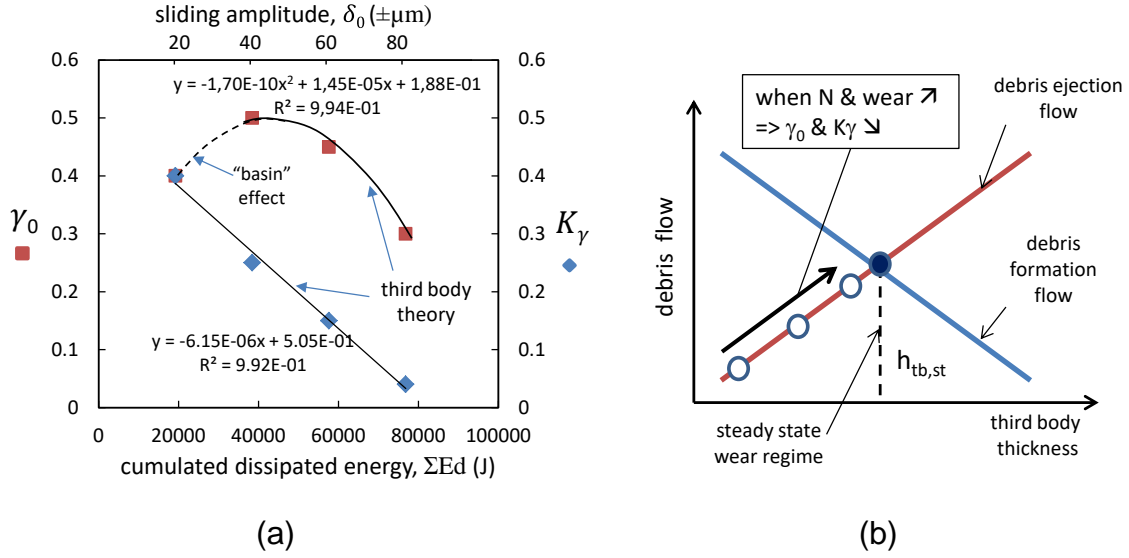


Fig. 13: a) evolution of the γ_0 and K_γ as a function of the accumulated friction energy ($R=40$ mm, $N=10^5$ cycles, $P=400$ N/mm, $f=0.5$ Hz, varying δ_g ; b) third body theory (after [31]): An increase of the third body debris layer thickness increases the debris ejection flow (more debris are ejected during each sliding sequence) but decreases the debris formation flow (more friction energy is consumed by the debris layer).

From this debris formation – debris ejection balance it can be explained why the conversion factor is high at the beginning of the test according that all the new debris are imputed in the debris layer, but converge to zero when the thickness of debris layer stabilizes. It is however surprisingly to note a non-monotonous evolution of the γ_0 parameter which displays a first rising at the beginning of the surface wear. Again this could be explained assuming the “basin” effect occurring on the plane surface which, trapping the debris layer promotes during a short period a small rising of γ_0 parameter. Regarding the K_γ coefficient, the linear decreasing toward a very small value (Fig. 13a) is consistent with fact that the debris layer, displays at the beginning a bell shape (Fig. 12), evolves inexorably toward a quasi-flat profile. Hence, the larger the surface wear, the flatter the friction energy density profile, the flatter the debris layer and consequently the flatter the $\gamma(x)$ distributions.

According that $\gamma(x)$ and therefore γ_0 and K_γ parameters depends on the surface wear extension, we proposed to formalize the evolution of these various parameters using a polynomial function of the accumulated friction energy:

$$\text{if } \Sigma Ed < \Sigma Ed_{th,\gamma_0} : \gamma_0 = A \times Ed^2 + B \times Ed + C \quad (32)$$

$$\text{if } \sum Ed > \sum Ed_{th,\gamma_0} : \gamma_0 = 0 \quad (33)$$

$$\text{if } \sum Ed < \sum Ed_{th,K_\gamma} : K_\gamma = D \times Ed + E \quad (34)$$

$$\text{if } \sum Ed > \sum Ed_{th,K_\gamma} : K_\gamma = 0 \quad (35)$$

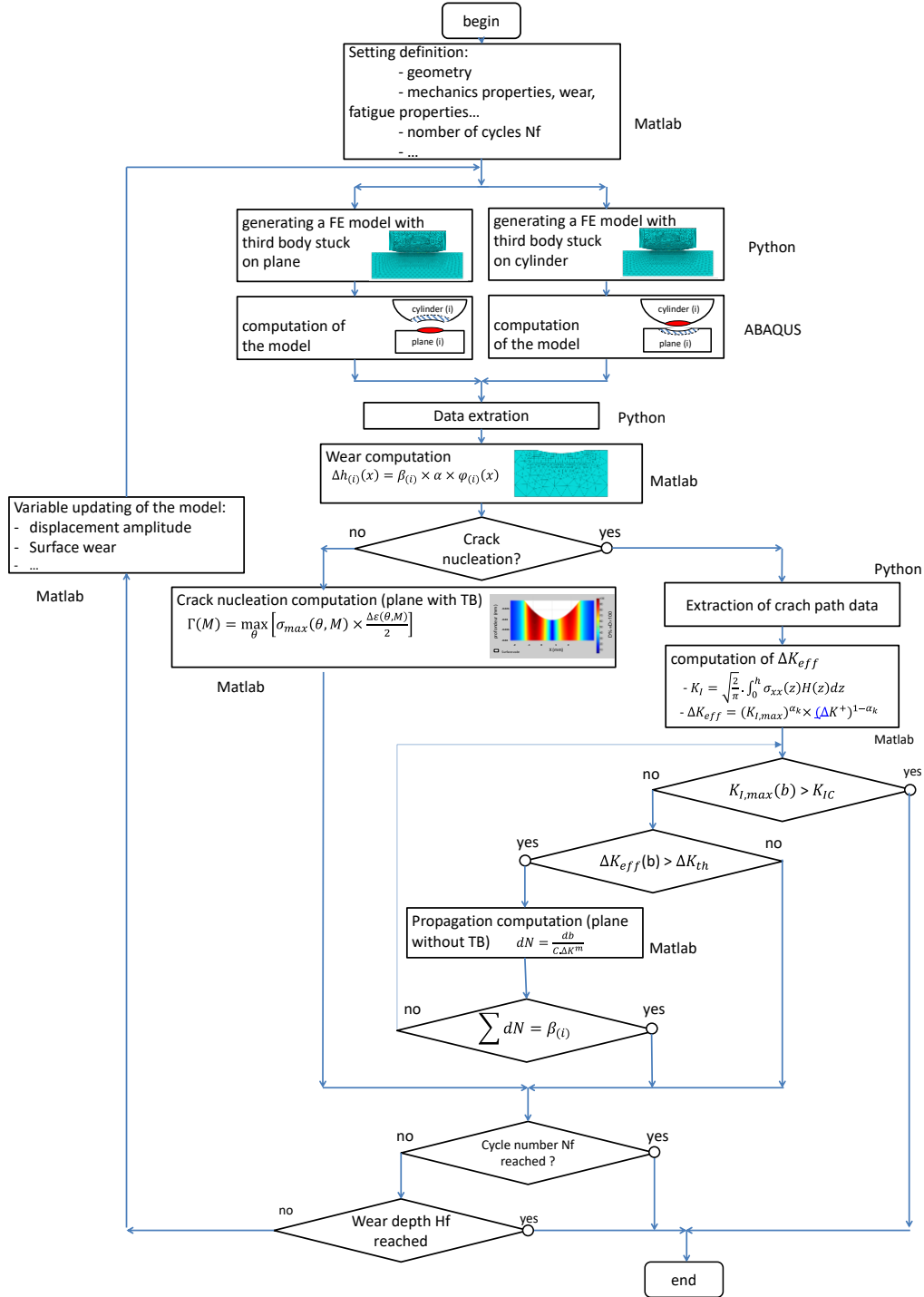


Fig. 14: global algorithm of the model.

Combined simulations of wear and cracking process in fretting fatigue

Both cracking and surface wear modeling are now combined through a single algorithm to simulate the fretting fatigue endurance as a function of the displacement amplitude. A schematic description of the global algorithm is illustrated in figure 14.

The model is able to formalize the crack nucleation, the crack propagation but also the surface wear taking into account the evolution of the debris layer. Crack nucleation is activated when the accumulated damage reaches 1, the crack arrest condition is achieved when ΔK_{eff} is under passing the ΔK_{th} threshold and failure is established when $K_{I,max}$ is higher than the K_{IC} fracture toughness. The fretting fatigue endurance (i.e. $N_F = N_N + N_P$) is computed considering the evolution of fretting fatigue stressing and the surface wear damages.

3. Results and discussion

3.1. Partial slip domain

Figure 15 illustrates the evolution of N_N and N_F as the function of the displacement amplitude δ^* . The difference between the two curves corresponds to the propagation period. The simulations were performed without surface wear simulations. Both crack nucleation and failure endurance curve display an asymptotic decreasing reaching minimum endurance values at the δ_t sliding transition (Fig. 15).

A rather good correlation with experiments is observed. The model which perfectly predicts the fretting fatigue endurance in first part of the partial slip domain $\delta^* < \delta_t/2 \approx 50 \mu\text{m}$, becomes slightly conservative next to the gross slip boundary. This very good correlation demonstrates *a posteriori* that almost no wear is generated under partial slip condition [33]. Former research works suggest that wear under partial slip conditions promotes geometry discontinuities at the sticking boundary inducing a sharp rising of the cracking risk [34]. These conclusions are fully contradicting the given observations. In fact, most of these numerical investigations consider the energy wear rate defined from gross slip conditions to estimate the surface wear damage generated under partial slip. Heredia et al [33] suggested that the sliding amplitude in partial slip sliding zones is so small that wear debris cannot be ejected from the interface. This implies that the real fretting wear rate under partial slip condition is much smaller than observed under gross slip and can even be

neglected. This tendency is presently confirmed given the very good correlation between the experimental fretting fatigue endurance.

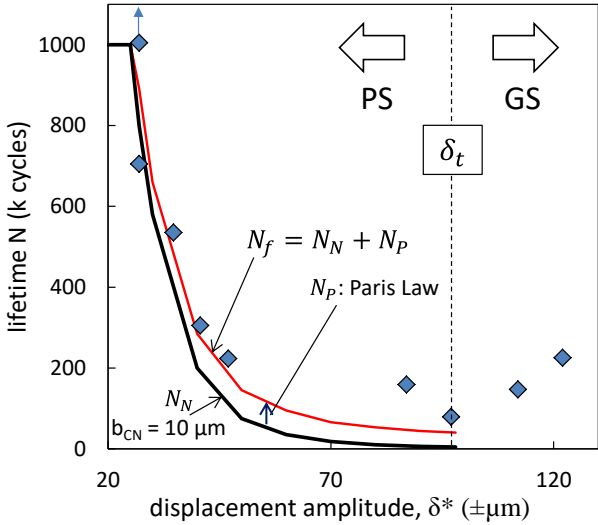


Fig. 15: Analysis of the fretting fatigue endurance under partial slip : Comparison between experiments (failure endurance) and simulations without surface wear consideration: N_N , crack nucleation fretting fatigue cycles (red full line), N_f , failure fretting fatigue cycles (: black full line) (35NCD16/S2 100, $R=40$ mm $P=400$ N/mm $\sigma_{fat}=400$ MPa, $R_{fat}=0.1$).

The relative difference between N_N and N_f which is very small in the first part of the partial slip domain (i.e. $\delta^* < \delta_t/2 \approx 50 \mu m$) (Fig. 15) shows that for low partial slip fretting stressing, the global endurance is mainly controlled by the crack nucleation process. However, by increasing the displacement amplitude and therefore the fretting stressing (i.e. $\delta_t/2 < \delta^* < \delta_t$) the crack nucleation is becoming faster and the proportion of endurance related to the propagation stage is rising. At the sliding transition, fretting cycles related to propagation (N_P) is nearly 3 times higher than the nucleation (N_N) period. On the other hand, the higher the displacement amplitude, the shorter the crack nucleation and finally the longer the relative period related to propagation.

3.2. Gross slip domain

Figure 16 compares the gross slip fretting fatigue endurance predicts by the 3 surface wear hypotheses: no surface wear (NW), wear without third body consideration (W) and wear with third body consideration (W&TB). As expected, the

model without wear displays constant and very low lifetimes. Indeed, without surface wear, the high Hertzian pressure and shear profiles are kept constant.

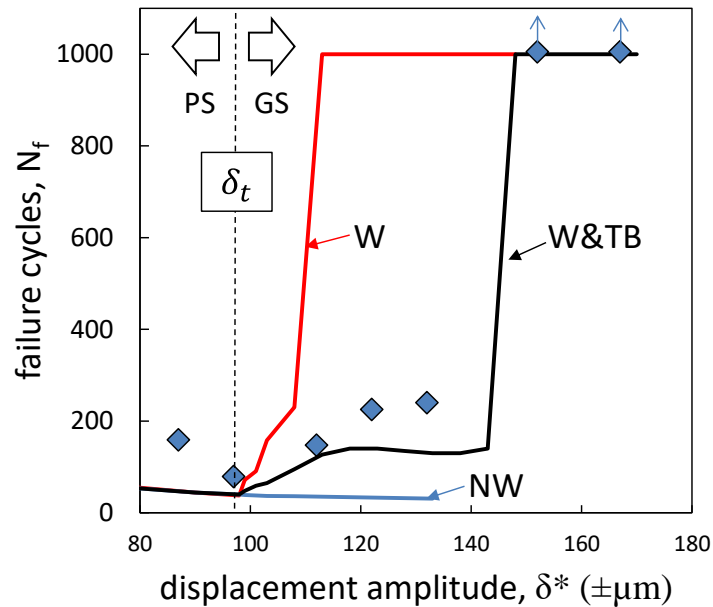


Fig. 16: Comparison of fretting fatigue endurance in gross slip condition: (♦) experiments versus simulations (NW : No Wear hypothesis; W : Wear without third body hypothesis; W&TB : Wear and Third Body hypothesis), (conditions: 35NCD16/ 52100, $R=40$ mm $P=400$ N/mm $\sigma_{fat}=400$ MPa, $R_{fat}=0.1$).

The model with wear simulation but without third body consideration critically overestimates the fretting fatigue lifetime. Finally, the best correlation is achieved by the model combining both surface wear and third body effect. To better interpret the effect of surface wear and debris layer a numerical investigation is performed for a illustrating $\delta_0 = \pm 10 \mu\text{m}$ (i.e. $\delta^* \approx \pm 110 \mu\text{m}$) gross slip condition.

3.2.1. Crack nucleation

Figure 17a&b compares the evolution of contact pressure profiles and related surface wear profiles given by the two simulations: wear without third body (W) and wear with third body (W&TB) respectively. Figure 17c displays the evolution of the maximum contact pressure as a function of the fretting cycles. It confirms that surface wear induces a fast decrease of contact pressure and promotes a significant extension of contact area. By contrast, the presence of third body mitigates such effects. By

concentrating the friction dissipation in the central part of the contact it reduces the lateral extension and maintains higher contact pressure.

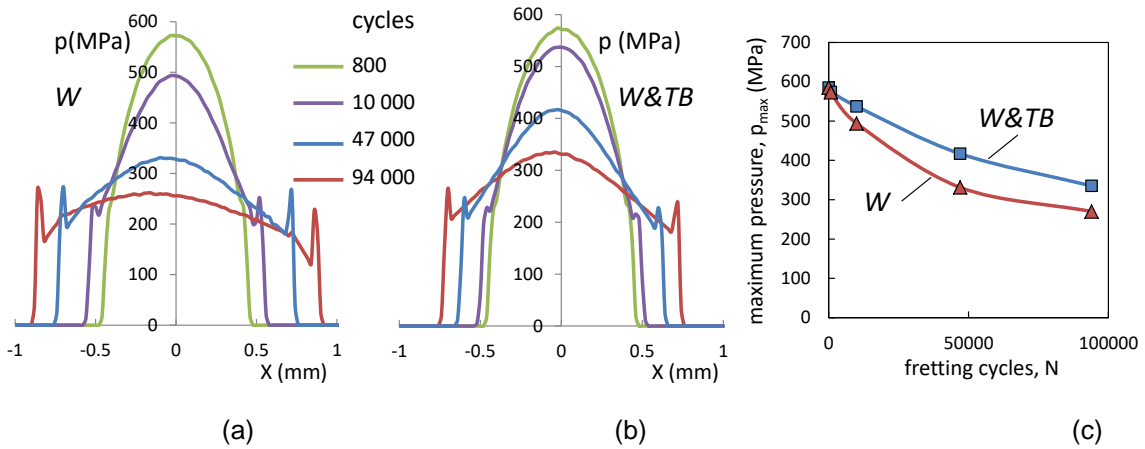


Fig. 17: Influence of surface wear on contact pressure simulations: (a) Evolution of pressure and worn profiles for different fretting cycles: comparison between plain wear (W) and wear combined with debris layer ($W\&TB$) hypotheses; (c) Evolution of the maximum pressure as a function of fretting cycles (35NCD16/52100, $R=40$ mm $P=400$ N/mm $\sigma_{fat}=400$ MPa, $R_{fat}=0.1$, $\delta_0=\pm 10$ μ m).

Figure 18a and 18b compare the SWT profiles for simulations with and without third body. As expected, higher Γ_{swt} values are computed when the surface wear simulations take into account the debris layer. Nevertheless, this effect is more visible when the fatigue stress is lower ($\sigma_{fat}=170$ MPa).

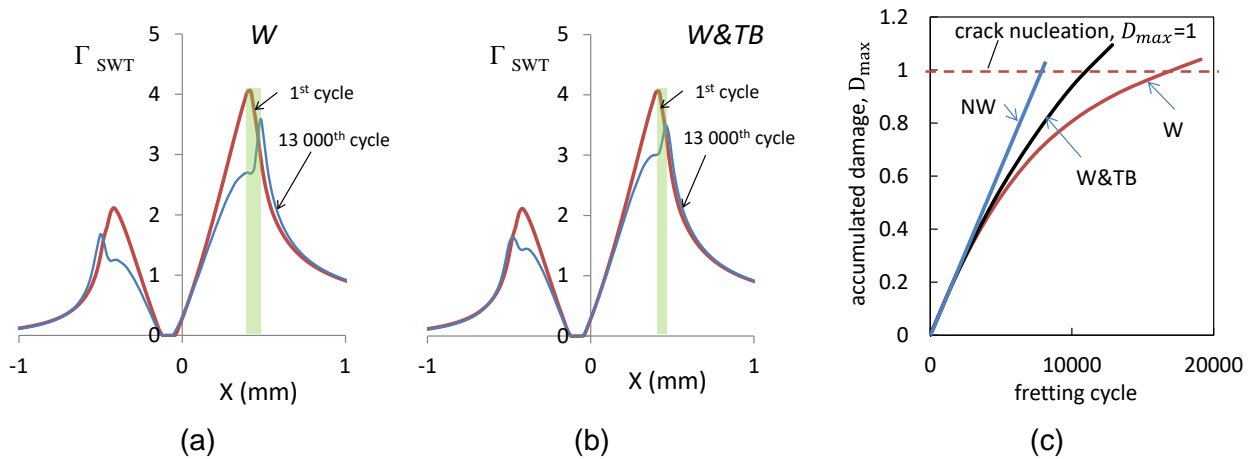


Fig 18: Comparison of SWT profiles at the critical distance below the surface ($l=30$ μ m) depending on the surface wear modeling: (a) simulation without third body (W); (b) simulation with third body layer ($W\&TB$); (c) Evolution of the cumulated damage given by the three hypotheses NW , W and $W\&TB$ (35NCD16/52100, $R=40$ mm $P=400$ N/mm $\sigma_{fat}=170$ MPa, $R_{fat}=0.1$, $\delta_0=\pm 10$ μ m)

Besides reducing the lateral extension, the cyclic stresses are localized in a more restricted lateral band at the trailing edge inducing a faster rising of the cumulated damage (Fig. 18c). If no wear is considered (NW), the cumulated damage rises linearly, inducing over conservative crack nucleation predictions and a short 9000 loading cycles endurance for the studied condition. Applying the plain surface wear hypothesis (W), a significant reduction of pressure and therefore fretting stressing is observed. The crack nucleation endurance rises up 20 000 fretting fatigue cycles which can be considered as a non-conservative prediction. An intermediate and more appropriated response is achieved applying surface wear with third body debris layer (W&TB). Using this approach, the crack nucleation is predicted around 11 000 loading cycles.

3.2.2. Crack propagation

Figure 19 displays the evolution of \bar{K}^* as the function of the projected crack length for a $\delta_0 = \pm 10 \mu\text{m}$ gross slip sliding condition. As expected from pressure field evolution, the fastest rising is given by the model which does not consider surface wear (NW). The slowest rising is provided by the plain wear modeling (W) whereas the combined wear and third body approach (W&TB) leads to an intermediate response.

Note that for the studied alloy, the short crack transition is very small, equivalent to the crack nucleation length ($\sim 10 \mu\text{m}$). Hence, if a crack nucleates, either it is immediately arrested ($\bar{K}^* < \Delta K_{th}$) or will propagate until failure ($\bar{K}^* > \Delta K_{th}$).

By contrast to other materials [35, 36], this fretting fatigue analysis does not require a short crack correction to establish the crack arrest situation. The Paris law is integrated and figure 19 compares the evolution of simulated crack length extension as a function of fretting fatigue cycles. As expected, the faster and over conservative crack propagation rate is given by the model without wear simulation (NW), the slower and non-conservative prediction is provided by the classical plain wear approach (W) whereas the combined wear and third body modeling leads to a more representative intermediate response. For the studied conditions, the crack propagation endurance is predicted at 38 000, 166 000 and 92 000 loading cycles respectively.

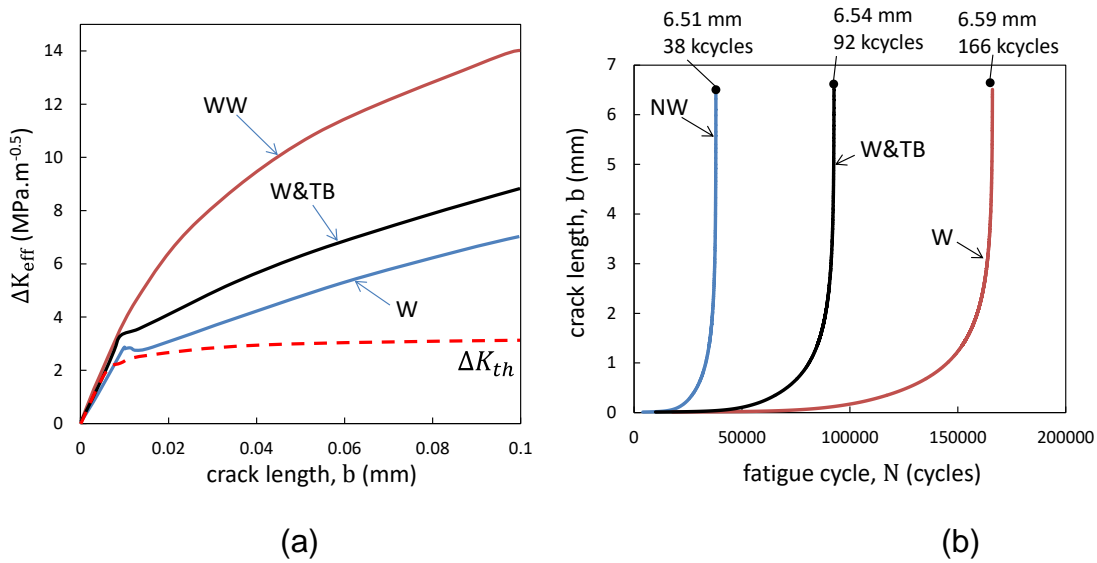


Fig. 19: Influence of surface wear hypothesis regarding crack propagation rate for a gross slip condition (i.e. 35NCD16/52100, $R=40$ mm $P=400$ N/mm $\sigma_{fat}=400$ MPa, $R_{fat}=0.1$, $\delta_0=\pm 10$ μ m): (a) Evolution of the \bar{K}^* versus projected crack length; (b) modeling of the extension rate integrating the Paris law.

3.3. Global response

Figure 15 and 16 suggest that the best fretting fatigue modeling consists in neglecting the surface wear under partial slip condition and considering a surface wear modeling taking into account debris layer under gross slip condition. This so called “PS(NW)-GS(W&TB)” strategy is now adopted to simulate both crack nucleation and failure endurance as a function of the displacement amplitude from partial to gross slip conditions (Fig. 20). The very good correlation with experiments confirms the stability of this approach. Both crack nucleation and failure boundaries almost appear superimposed in the closed partial slip domain ($\delta^* < \delta_t/2 \pm 50$ μ m). A larger difference is observed in the second part of the partial slip domain next to the gross slip transition (i.e. $\pm 50 \mu$ m $< \delta^* < \pm 97$ μ m). The model also well predicts the stair case evolution observed just above the gross slip transition as well as the infinite endurance threshold around $\delta^* \approx \pm 140 \mu$ m. This endurance discontinuity is related to the activation of a crack arrest condition itself induced by a wear-softening of contact stressing. Above $\delta^* \pm 150$ μ m the model suggests a non-nucleation condition induced by the very fast surface wear which is removing the incipient cracks nucleated during the initial high pressure period. Surface wear is also reducing drastically the contact pressure so that form successive crack nucleation is

also prevented. This non-nucleation scenario is confirmed by cross-section expertise of gross slip unbroken fretting fatigue specimens (i.e. test c2, Fig.5) underlying that no cracks longer than 10 μm were observed for displacement amplitudes longer than $\pm 140 \mu\text{m}$.

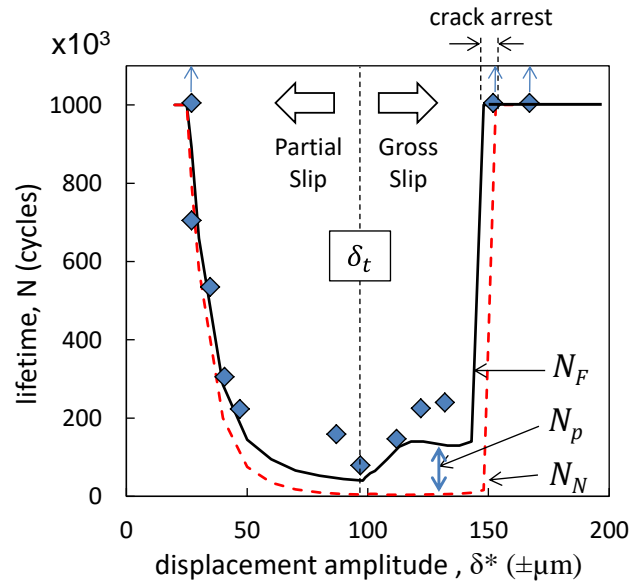


Fig 20: Evolution of crack nucleation (N_N) and failure (N_F) endurances predicted by the PS(NW)-GS(W&TB) fretting fatigue modeling. Comparison with experimental failure endurances (35NCD16/S2 100, $R=40 \text{ mm}$ $P=400 \text{ N/mm}$ $\sigma_{fat}=400 \text{ MPa}$, $R_{fat}=0.1$).

It is interesting to note that the model is systematically conservative which is required for any industrial application. To better illustrates the relative crack nucleation and crack propagation periods, both computed N_p and N_N values are plotted versus δ^* on figure Fig.20a whereas Fig. 20d displays the corresponding evolution of the non-dimensional N_p/N_N ratio. After this plotting, 4 domains can be identified. The first one concerns the partial slip domain characterized by a continuous rising of the N_p/N_N ratio until the gross slip transition. Note that below $\delta_t/2$ (i.e. $\pm 50 \mu\text{m}$) the crack nucleation period is longer than the propagation one. Above the gross slip transition, the domain II is characterized by a non-monotonous evolution of the N_p/N_N ratio displaying a fast rising until a maximum value around $N_p/N_N = 35$ around $\delta^* = \pm 120 \mu\text{m}$, followed by a linear decrease until the infinite life time boundary ($\delta^* = \pm 140 \mu\text{m}$). Then, in domain III, the N_p/N_N ratio displays a very discontinuous behavior. From $\delta^* = \pm 140 \mu\text{m}$ to $\pm 150 \mu\text{m}$ (domain IIIa), the infinite endurance is here driven by a crack arrest condition which implies that the N_p/N_N ratio tends to infinity.

Whereas above $\delta^* = \pm 150\mu m$ (domain IIIb), the infinite fretting fatigue endurance is controlled by a non-nucleation crack condition which in turn implies that N_P/N_N converges to zero.

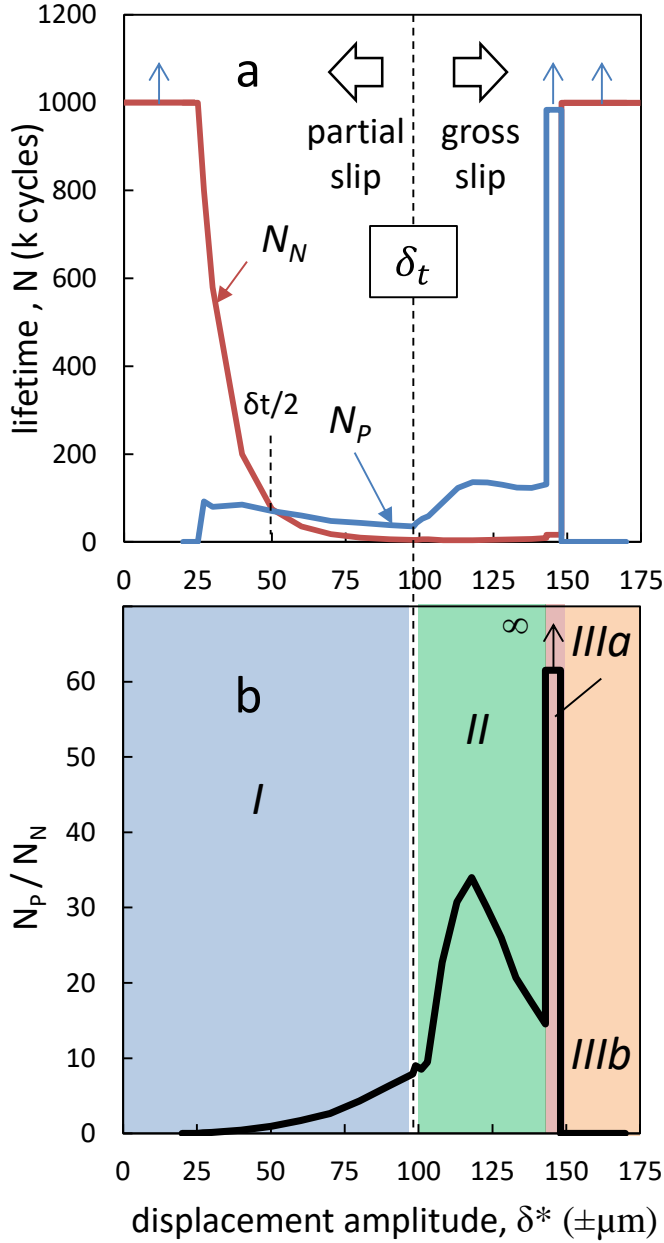


Fig. 21: Comparative (a) crack nucleation and crack propagation as a function of displacement amplitude; b) ratio N_P/N_N as a function of displacement amplitude.

Using the N_P/N_N approach, optimized palliative strategies may be adopted depending on the imposed displacement amplitude. For instance, surface coating can be adopted to prevent crack nucleation whereas shot peening compressive stress fields may be considered to limit the crack propagation extension.

3.4. Fretting Fatigue chart modeling

Former $Q^* - \sigma$ fretting fatigue chart was previously introduced to discriminate crack nucleation, crack arrest and failure domains as function the fretting (i.e. tangential force) and fatigue loadings [36]. However this approach was limited to the infinite endurance condition and restricted to partial slip situations.

Having the possibility to simulate both surface wear and cracking processes, it appears interesting to extend this approach whatever the sliding condition including a finite endurance description. The purpose of the following analysis consists in providing an extended DS (i.e. Displacement (δ^*) - fatigue Stress (σ_{fat})) fretting fatigue damage chart where cracking but also wear phenomena could be captured whatever the partial or gross slip configuration. The principle of this approach is illustrated in figure 22 where the displacement condition is formalized using the non-dimensional δ^*/δ_t ratio.

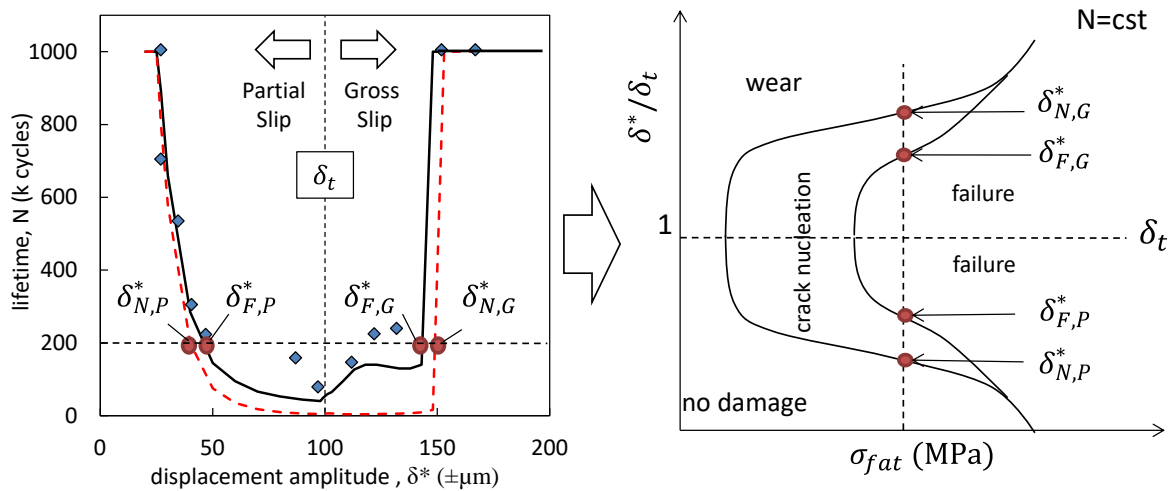


Fig. 22 Fretting Fatigue chart: Illustration of the procedure used to establish the DS (i.e. $\delta^* - \sigma$) fretting fatigue damage chart (application from the studied “U-shape” endurance curve).

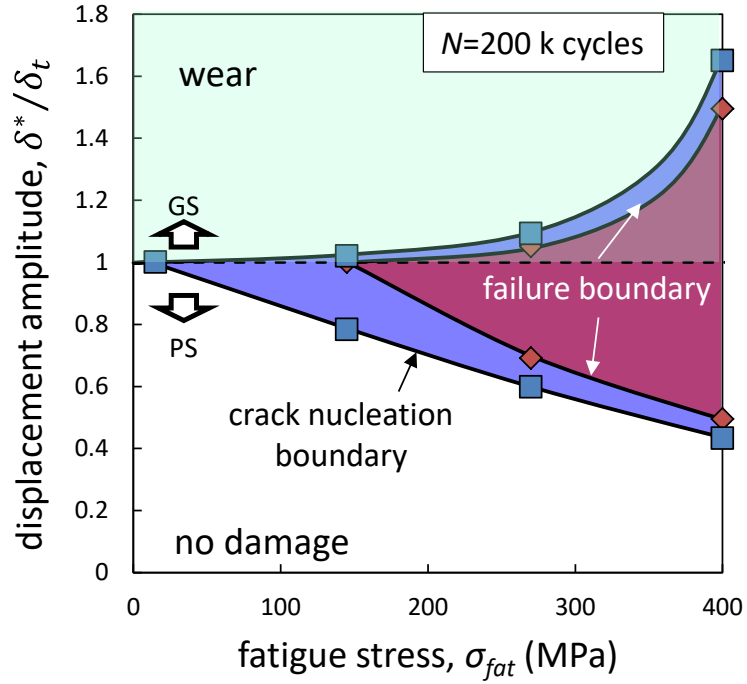
To establish the DS fretting fatigue chart, we need to define for a given fatigue stress and a given test duration, the following 4 key displacement amplitudes which are respectively:

- $\delta_{N,P}^*$: the partial slip displacement amplitude related to the crack nucleation activation,
- $\delta_{F,P}^*$: the partial slip displacement amplitude related to the specimen failure,

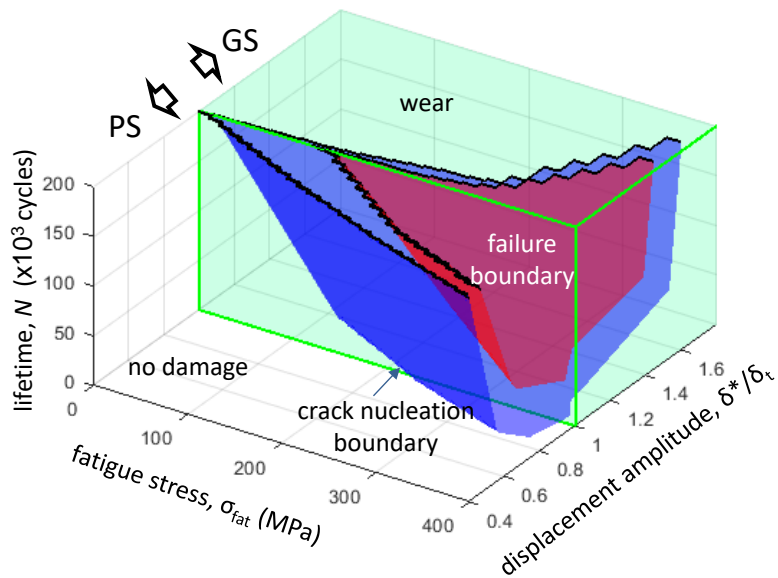
$\delta_{F,G}^*$: the gross slip displacement amplitude above which failure is no more observed,;
 $\delta_{N,G}^*$: the gross slip displacement amplitude above which crack nucleation is no more observed.

Figure 22, illustrates the procedure used to extract these 4 key displacement amplitudes. For the studied condition and a test duration established at 200.10^3 cycles, it was found $\delta_{N,P}^* = 40 \mu\text{m}$ $\delta_{F,P}^* = 45 \mu\text{m}$ $\delta_{F,G}^* = 140 \mu\text{m}$ and $\delta_{N,G}^* = 150 \mu\text{m}$.

The complete description of DS (i.e. $\delta^* - \sigma_{fat}$) fretting fatigue chart from experimental investigation is very long and fastidious. However, using the given FEM computations, validated using a restricted set of experiments, such a global description could easily be achieved. Figure 23 (a) illustrates the DS fretting fatigue chart simulated for $N = 200.10^3$ fretting fatigue cycles. The crack nucleation boundary in partial slip displays a linear decreasing. Indeed, former investigations assuming elastic hypothesis suggest that contact stresses are proportional to the tangential force Q^* and consequently the crack nucleation boundary decreases linearly with the displacement amplitude δ^* . The evolution of failure boundary is less linear according that propagation implies to integrate the Paris law which is a power law function. It is interesting to note that the higher the fatigue stress, the shorter the propagation stage and therefore the narrow the distance between the crack nucleation and failure boundaries. In gross slip domain, both crack nucleation and failure boundaries display an exponential rising evolution with the fatigue stress σ_{fat} . This mapping analysis suggests that the contact stress reduction induced by surface wear is fast enough to prevent crack nucleation and failure. Up to $\sigma_{fat} = 200 \text{ MPa}$, both crack nucleation and failure boundaries are nearly superimposed following the partial slip / gross slip transition. When the fatigue stress increases, the relative influences of contact stress and therefore surface wear effect is decreasing. Fatigue stresses are not influenced by the surface wear which can explain the extension of failure and crack nucleation domains when the fatigue stress increases. Hence, this $\delta^* - \sigma_{fat}$ numerical investigation allows us to better interpret the benefit effect of gross slip surface wear regarding fretting fatigue cracking process.



(a)



(b)

Fig. 23: Illustration of the proposed fretting fatigue chart methodology: (a) DS (i.e. $\delta^* - \sigma$) fretting fatigue chart as function of displacement and fatigue stress for a given 200 000 cycles; (b) Extended DSN (i.e. $\delta^* - \sigma_{fat} - N$) fretting fatigue chart displaying the damage evolution as function of displacement amplitude (S), fatigue stress (S) and fretting fatigue cycles (N) (contact condition: 35NCD16/52100, $R=40$ mm $P=400$ N/mm, $R_{fat}=0.1$, $\delta_t=97$ μ m).

This numerical fatigue-fatigue damage chart can also be extended by investigating the effect of test duration (i.e. N loading cycles). Figure 23b illustrates the so called DSN chart (i.e. $\delta^* - \sigma_{fat} - N$) extrapolated from the given model. Using this 3D representation, the time evolution of non-damage, crack nucleation, failure and surface wear damage domains can be depicted and quantified. Such a dynamical representation appears as a very useful designing strategy to optimize fretting fatigue assemblies.

Deeper investigations are now required to extend this approach to capture other aspects like contact size, contact geometry, fatigue stress ratio but also surface treatments including coatings and shot peening treatments. Another aspect concerns the fatigue properties of the material regarding crack nucleation and crack propagation. The studied 35NCD16 displays a rather low ΔK_{th} threshold which in return reduces the crack arrest domain. Hence there is a key interest to investigate materials displaying higher ΔK_{th} values like XC38 alloy [36, 37]. To conclude, the given “PS(NW)-GS(W&TB)” fretting fatigue modeling strategy and related DSN damage chart representation appear as a pertinent approaches to predict the fretting fatigue damages whatever the fretting sliding conditions and material properties.

4. Conclusion

The mechanisms of fretting fatigue damage of 2D cylinder/plane (35NCD16/52100), interface was extensively investigated combining experiments and simulations. From this research study the following points emerge:

- Using a double actuator fretting fatigue test machine, the evolution of the fretting fatigue endurance versus the applied displacement δ^* was investigated for a constant fatigue stress. A typical “U shape” endurance curve is obtained displaying a decreasing of the failure endurance in partial slip until a minimum value at the partial slip/gross slip transition δ_t . Then above this value, gross slip surface wear is activated promoting a rising of the fretting fatigue endurance until the material fatigue limit.
- A complete FEM-Python-Matlab code is established, combining crack nucleation crack propagation, surface wear and debris layer simulations. Using this code, the competition between surface wear and cracking phenomena in gross slip regime can be formalized. The FE model was

updated using a System Accommodation Part (SAP) allowing a direct correlation between experimental and numerical displacement amplitudes.

- An original strategy is established to calibrate the model using low cost plain fretting test. A SWT crack nucleation fatigue law taking into account the contact stress gradient effect is extracted from the post processing analysis of plain fretting tests performed at different test durations. The crack nucleation length is related to the transition from short to long crack propagation regime. The friction energy wear coefficient but also the debris conversion parameters are extracted from an equivalent post processing analysis of gross slip plain fretting tests.
- The analysis confirms rather good predictions of the partial slip fretting fatigue endurance even if surface wear is not considered in the simulations (i.e. PS(NW) hypothesis). This confirms that even if there is friction dissipation under partial slip, the sliding amplitudes are so small that wear debris can not be ejected. After the third body theory, the debris flow ejection converges to zero as well as the fretting wear rate. The gross slip investigation suggests that the best predictions are achieved if the wear model is combined with a third body debris layer simulation (i.e. GS(W&TB)). The no wear hypothesis is over-conservative because it does not consider stress reduction induced by surface wear contact extension. Alternatively, the plain wear simulation (i.e. without third body consideration) over-estimates the lateral contact extension and contact pressure reduction inducing dangerous non conservative predictions. Hence the so called “PS(NW)-GS(W&TB)” numerical modeling strategy is established to predict the fretting fatigue endurance whatever the sliding condition.
- Global DS (i.e. $\delta^* - \sigma_{fat}$) and extended DSN (i.e. $\delta^* - \sigma_{fat} - N$) numerical fretting fatigue charts are finally introduced to display through a useful description the evolution of fretting different damages (wear and cracking) as a function of the displacement amplitude (δ^*), fatigue stress (σ_{fat}) and test duration (N).

Future developments will consist of better formalizing surface treatment effects, contact geometry [38] (i.e. sphere/plane, punch/plane contact), variable loading conditions [39], but also rheological properties of third body.

References:

- [1] R.B. Waterhouse, Fretting Fatigue, AppliedScience Publishers; 1981.
- [2] L. Vincent, Y. Berthier, M. Godet, Testing methods in fretting fatigue: a critical appraisal, in: Standardization of fretting fatigue test methods and equipment, STP,1159 (1992) 33–48
- [3] O. Vingsbo, S. Soderberg, On fretting maps, Wear 126 (1988) 131–147.
- [4] D. Taylor, Geometrical effects in fatigue: a unifying theoretical model. International Journal of Fatigue 21 (1999) 413–420.
- [5] S. Fouvry, Ph Kapsa, L. Vincent, A multiaxial fatigue analysis of fretting contact taking into account the size effect, ASTM STP 1367 (2000) 167–182.
- [6] J.A. Araujo, D. Nowell, The effect of rapidly varying contact stress fields on fretting fatigue, Int J Fatigue 24 (2002) 763–775.
- [7] H. Kitagawa, S. Takahashi, Application of fracture mechanics to very small cracks or the cracks in the early stage, ASTM, (1976) 627–630.
- [8] M. El Haddad, K. Smith, T. Topper, Fatigue crack propagation of short cracks, J. Engng Mater Technol 101 (1979) 42–46.
- [9] J.J. Madge, S.B. Leen, I.R. McColl, P.H. Shipway, Contact-evolution based prediction of fretting fatigue life: effect of slip amplitude, Wear 262 (9–10) (2007) 1159–1170.
- [10] F. Shen, W. Hu, Q. Meng, A non-local approach based on the hypothesis of damage dissipation potential equivalence to the effect of stress gradient in fretting fatigue, Int J Fatigue 90 (2016) 125–138.
- [11] S.M. O'Halloran, P.H. Shipway, A.D. Connaire, S.B. Leen, A.M. Harte, A combined wear-fatigue design methodology for fretting in the pressure armour layer of flexible marine risers, Tribology International 117, (2018) 141–151.
- [12] P. Arnaud, S. Fouvry, S. Garcin, Wear rate impact on Ti-6Al-4V fretting crack risk: experimental and numerical comparison between cylinder/plane and punch/plane contact geometries, Tribology International 108 (2017) 32-47.
- [13] J. Ding, I.R. McColl, S.B. Leen, P.H. Shipway A finite element based approach to simulating the effects of debris on fretting wear, Wear 263 (2007) 481-491.
- [14] P. Arnaud, S. Fouvry, A dynamical FEA fretting wear modeling taking into account the evolution of debris layer, Wear 412-413 (2018) 92-108.
- [15] L. J. Fellows, D. Nowell, D.A. Hills, On the initiation of fretting fatigue cracks, Wear 205 (1997) 120-129.

- [16] H. Mohrbacher, B. Blanpain, J.P. Celis, J.R. Roos, L. Stals, M. Van Stappen, Oxidational wear of TiN coatings on tool steel and nitrided tool steel in unlubricated fretting, *Wear* 188 (1995) 130-137.
- [17] S. Fouvry, P. Kapsa, L. Vincent, Quantification of fretting damage, *Wear* 200 (1996) 186–205.
- [18] S. Fouvry, P. Arnaud, A. Mignot, P. Neubauer, Contact size, frequency and cyclic normal force effects on Ti–6Al–4V fretting wear processes: an approach combining friction power and contact oxygenation, *Tribology International* 113 (2017) 460-473.
- [19] J. Meriaux, S. Fouvry, K.J. Kubiak, S. Deyber, Characterization of crack nucleation in TA6V under fretting–fatigue loading using the potential drop technique, *International Journal of Fatigue* 32 (2010) 1658-1668.
- [20] M. C. Dubourg, A. Chateauminois, B. Villechaise, In situ analysis and modeling of crack initiation and propagation within model fretting contacts using polymer materials, *Tribology International* 36 (2003) 109-119
- [21] K. N. Smith, P. Watson, T.H. Topper, A stress-strain function for the fatigue of metals, *J Mater* 5 (4) (1970) 767–778.
- [22] M. Szolwinski, T.N. Farris, Observation, analysis and prediction of fretting fatigue in 2024-T351 aluminium alloy, *Wear* 221 (1998) 24–36.
- [23] S. Fouvry, H. Gallien, B. Berthel, From uni-to multi-axial fretting-fatigue crack nucleation: Development of a stress-gradient-dependent critical distance approach, *Int. J. Fatigue* 62 (2014) 194–209.
- [24] H.F. Bueckner, A novel principle for the computation of stress intensity factors, *Zeitschrift fuer Angewandte Mathematik & Mechanik* 50 (1970) 529-546.
- [25] C. Navarro, J. Vázquez, J. Domínguez, A general model to estimate life in notches and fretting fatigue, *Engineering Fracture Mechanics* 78 (2011) 1590–1601
- [26] A. de Pannemaecker, S. Fouvry, M. Brochu, J.Y. Buffiere, Identification of the fatigue stress intensity factor threshold for different load ratios R: From fretting fatigue to C(T) fatigue experiments, *Int J Fatigue* 82 (2016) 211-225.
- [27] D. Kujawski, A fatigue crack driving force parameter with load ratio effects. *International Journal of Fatigue* 23 (2001) 239–246.

- [28] G. Gallet, H.P. Lieurade, Influence de la structure métallographique d'un acier au nickel- chrome-molybdène sur son comportement en fatigue plastique, Mémoires Scientifiques, Revue Métallurgie (1976) 219-239.
- [29] L. Johansson, Numerical simulation of contact pressure evolution in fretting, J. Tribol. 116 (1994) 247–254.
- [30] C. Paulin, S. Fouvry, C. Meunier, Finite element modelling of fretting wear surface evolution: Application to a Ti–6Al–4V contact, Wear 264 (2008) 26-36.
- [31] Y. Berthier, Maurice Godet's third body, Tribology Series, 31 (1996) 21–30.
- [32] N. Fillot, I. Iordanoff, Y. Berthier, Wear modeling and third body concept, Wear 262 (2007) 949-957.
- [33] S. Heredia, S. Fouvry, Introduction of a new sliding regime criterion to quantify partial, mixed and gross slip fretting regimes: correlation with wear and cracking processes, Wear 269 (2010) 515–524.
- [34] J. Ding, S. B. Leen, I. R. McColl, The effect of slip regime on fretting wear-induced stress evolution, International Journal of Fatigue 26 (2004) 521-53.
- [35] J.A. Araújo, D. Nowell, Analysis of pad size effects in fretting fatigue using short crack arrest methodology, Int. Journal of Fatigue 21 (1999) 947–56.
- [36] S. Fouvry, K. Kubiak, Introduction of a fretting-fatigue mapping concept: development of a dual crack nucleation – crack propagation approach to formalize fretting-fatigue damage Int. J. Fatigue 31 (2009) 250-262.
- [37] A. de Pannemaecker, S. Fouvry, J.Y. Buffiere, Reverse identification of short–long crack threshold fatigue stress intensity factors from plain fretting crack arrest analysis, Eng. Fract. Mech.134 (2015) 267-285.
- [38] J. Vázquez, C. Navarro, J. Domínguez, A model to predict fretting fatigue life including residual stresses, Theoretical and Applied Fracture Mechanics 73 (2014) 144–15.
- [39] G. Rousseau, C. Montebello, Y. Guilhem, S. Pommier, A novel approach to model fretting-fatigue in multiaxial and non-proportional loading conditions, International Journal of Fatigue 126 (2019) 79-89.
- [40] A. Viat, G. Guillonéau, S. Fouvry, G. Kermouche, S. Sao Joao, J. Wehrs , J. Michler , J. F. Henne, Brittle to ductile transition of tribomaterial in relation to wear response at high temperatures, Wear 392–393 (2017) 60–68.